Rapid trans-crustal magma movement under Iceland

Euan J. F. Mutch[1*], John Maclennan[1], Oliver Shorttle[1,2], Marie Edmonds[1] & John F. Rudge[3]

[1]*Department of Earth Sciences, University of Cambridge, Downing Street, Cambridge, CB2 3EQ, United Kingdom*

[2]*Institute of Astronomy, University of Cambridge, Madingley Road, Cambridge, CB3 0HA, United Kingdom*

[3]*Bullard Laboratories, Department of Earth Sciences, University of Cambridge, Madingley Road, Cambridge CB3 0EZ, UK*

Supplementary Figures

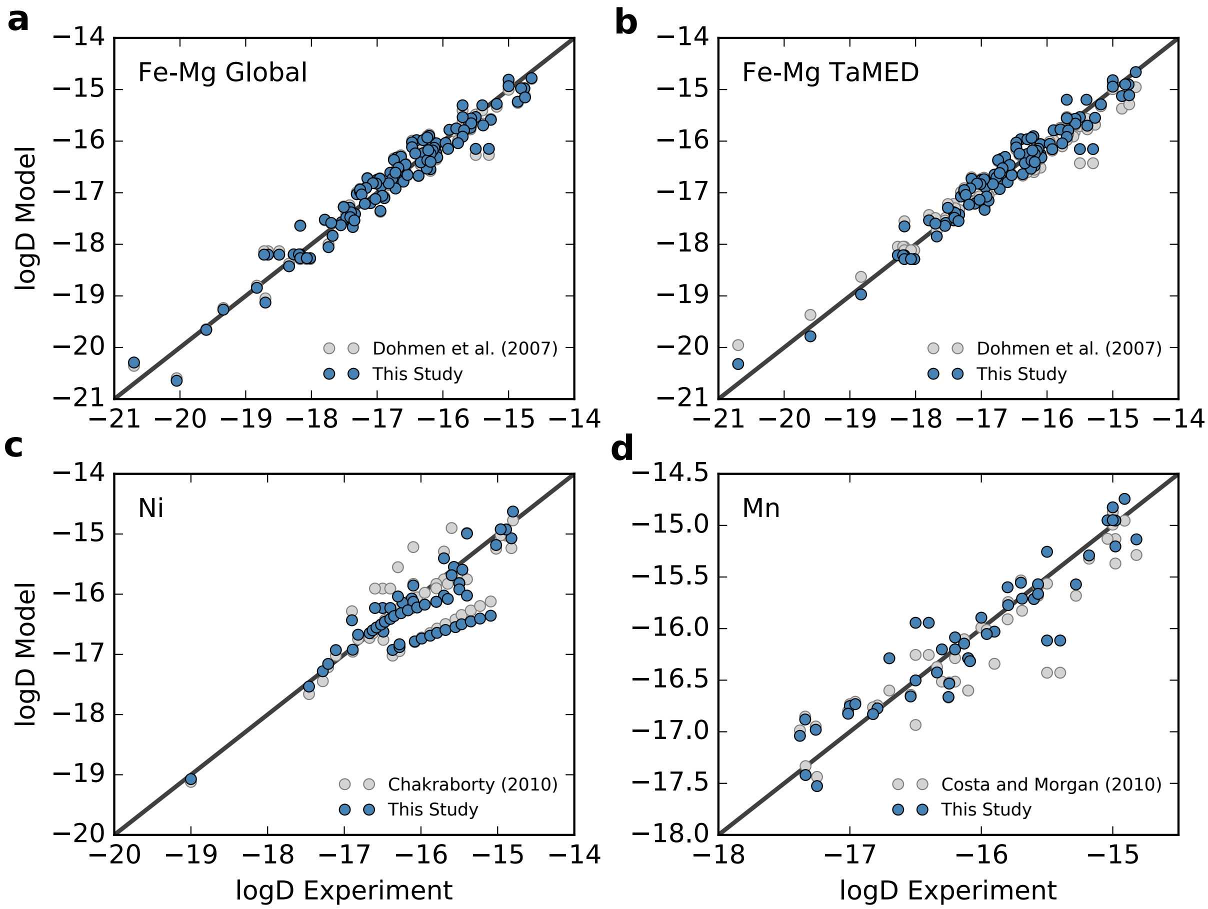

Supplementary Fig. 1: Assessing the performance of the olivine diffusion model multivariate regressions used in this study. Plots showing the model predictions of this study's olivine diffusion model multivariate regressions (blue circles) and those of previous studies[32,33,67,68] (grey circles) when applied to the calibrant experimental database. The black lines are 1:1 lines. **a,** Global Fe-Mg models **b,** TaMED mechanism for Fe-Mg exchange; **c,** Ni diffusion in olivine; **d,** Mn diffusion in olivine. The regressions of this study can retrieve the experimental diffusion coefficients within 0.5 log units, and are similar to diffusion equations of previous studies. In some cases, the models of this study outperforms the predictive power of previous calibrations, as is the case for Ni.

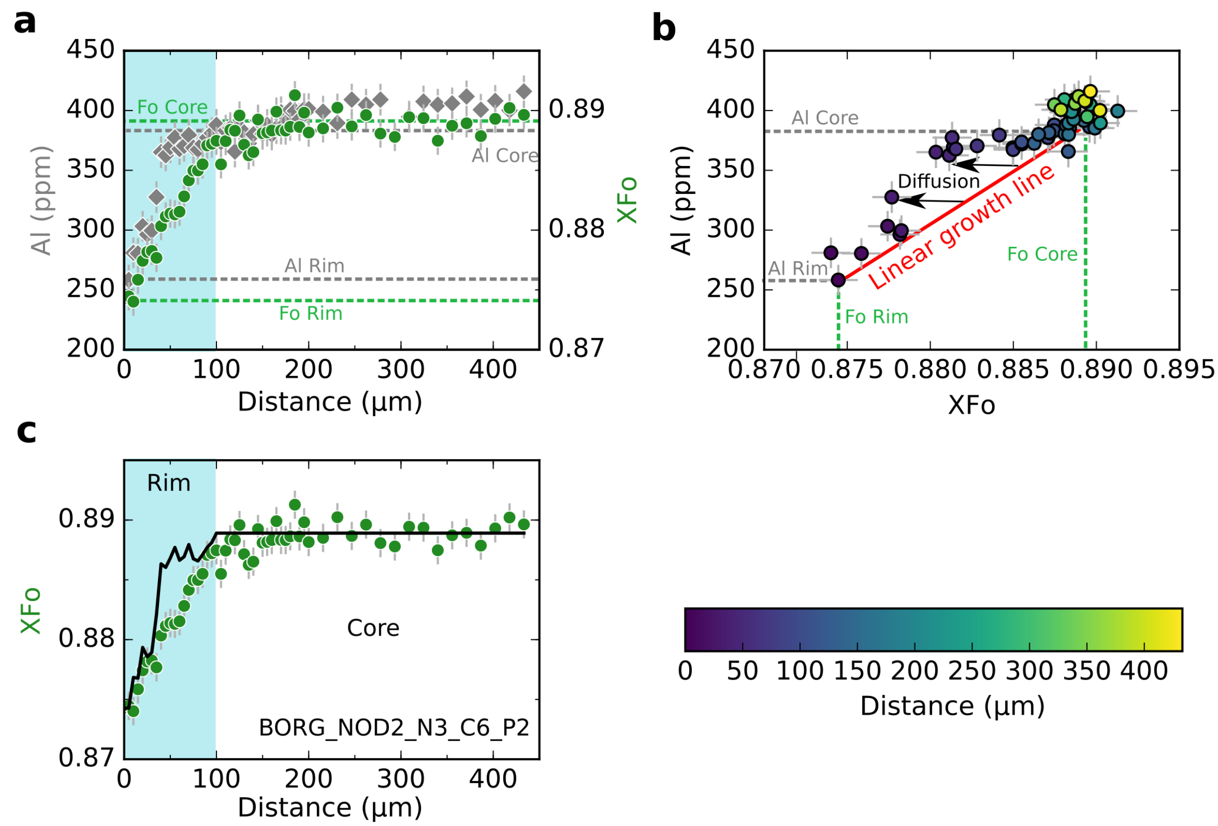

Supplementary Fig. 2: Constraining initial conditions for Al-decoupled olivine crystals. Plots showing how Al profiles were used to constrain the initial conditions for elemental diffusion modelling in olivine. This example is for sample BORG_NOD2_N3_C6_P2, which displays diffusive elemental decoupling between Al and forsterite content (X_{Fo}). **a,** shows X_{Fo} (green points) and Al (grey diamonds) profiles. The position of the rim was determined by the place where Al content starts to decrease from a plateau (marked by the light blue region). The core and rim compositions for these two elements were then selected as shown by the green and grey dashed lines. Rim compositions were chosen at the edge of the crystal, and core compositions were selected based on where the profiles flatten out (accounting for analytical uncertainties). **b,** shows these compositions plotted up in X_{Fo} vs. Al space with points being colour-coded based on distance. A linear regression between the picked rim and core compositions was then conducted (red line) and was used to represent growth. Deviation from this line was assumed to be due to diffusion, as shown by the arrows. The arrows are horizontal because Al is taken to be immobile[24,25], so diffusive modification will be only occur via Fe-Mg interdiffusion. Therefore the initial conditions for X_{Fo} were then produced by converting the Al compositions into X_{Fo} using this linear calibration curve (known as the linear growth curve). This was done only for the points defined in the rim region. Points outside of this zone were assigned the core X_{Fo}. **c,** shows these calculated initial conditions relative to the forsterite profile as a black line. Error bars are 1σ uncertainties from repeat measurements of San Carlos olivine secondary standards.

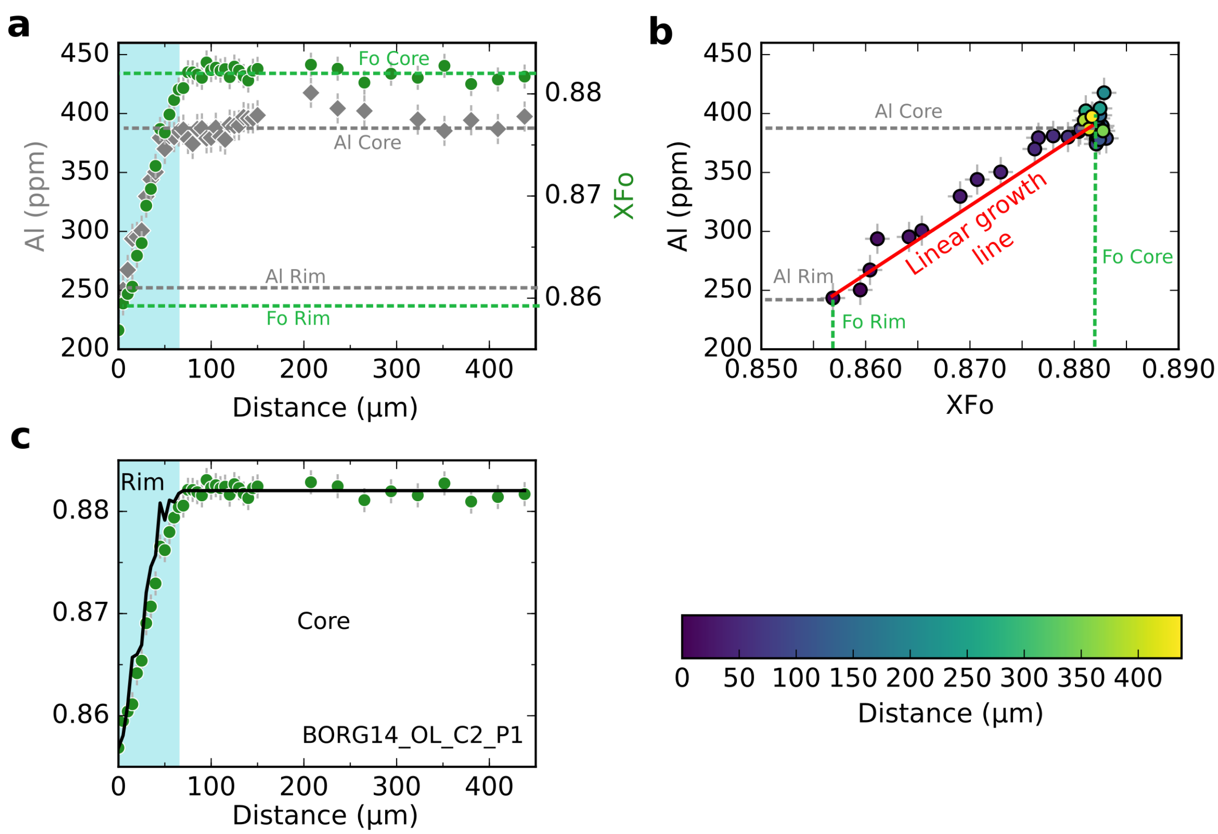

Supplementary Fig. 3: Constraining initial conditions for growth-dominated olivine crystals. Plots showing how Al profiles were used to constrain the initial conditions for elemental diffusion modelling in olivine. This example is for sample BORG14_OL_C2_P1, which displays limited diffusive elemental decoupling between Al and forsterite content (X_{Fo}), and is thus considered to be dominantely be growth controlled. **a,** shows X_{Fo} (green points) and Al (grey diamonds) profiles. The position of the rim was determined by the place where Al content starts to decrease from a plateau (marked by the light blue region). The core and rim compositions for these two elements were then selected as shown by the green and grey dashed lines. Rim compositions were chosen at the edge of the crystal, and core compositions were selected based on where the profiles flatten out (accounting for analytical uncertainties). **b,** shows these compositions plotted up in X_{Fo} vs. Al space with points being colour-coded based on distance. A linear regression between the picked rim and core compositions was then conducted (red line) and is used to represent growth. There is very little deviation from this line suggesting that the influence of diffusion was limited. The initial conditions for forsterite were then produced by converting the Al compositions into forsterite contents using the linear growth curve. This was done only for the points defined in the rim region. Points outside of this zone were assigned the core X_{Fo} value. **c,** shows these calculated initial conditions relative to the forsterite profile as a black line. Error bars are 1σ uncertainties from repeat measurements of San Carlos olivine secondary standards.

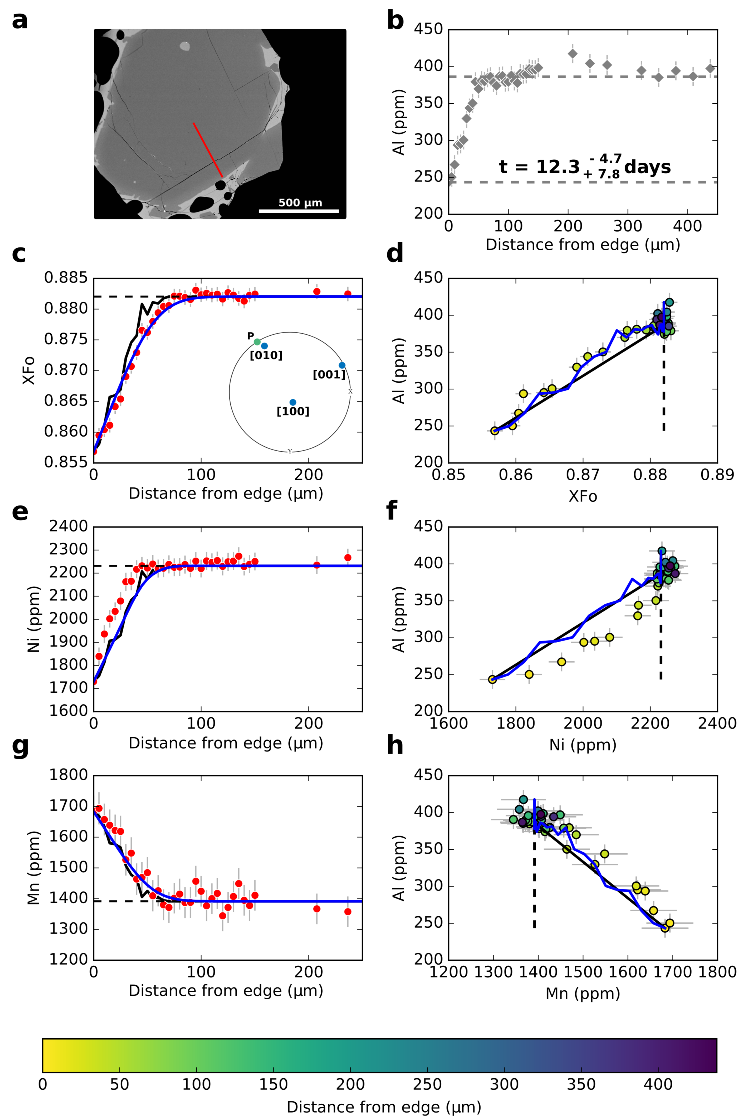

Supplementary Fig. 4: Data, initial conditions and model fits for sample BORG14_OL_C2_P1. **a,** Backscattered electron (BSE) image of the analysed olivine crystal with the location of the EPMA profile (red line). **b,** EPMA profile of Al. The grey dashed lines show selected core and rim compositions that were used to calibrate growth-controlled initial conditions for the diffusion modelling. The timescale shown is the median crystal residence time obtained from the Nested Sampling Bayesian inversion whilst simultaneosuly fitting Fo, Ni and Mn diffusion profiles. **c,** EPMA profile of mole fraction forsterite content (X_{Fo}) shown in red. Inset is an equal area pole figure of the crystal showing the orientation of the main crystallographic axes (blue points) relative to the profile (green point marked 'P'). **d,** X_{Fo} vs. Al cross-plot. **e,** EPMA profile of Ni shown in red. **f,** Ni vs. Al cross-plot. **g,** EPMA profile of Ni shown in red. **h,** Mn vs. Al cross-plot. Blue curves in **c**-**h** are maximum likelihood best fit model curves from the Bayesian Inversion corresponding to the time shown in **b**. The black lines and curves in **c**-**h** show the growth-controlled initial conditions based on a linear calibration between Al and the element of interest. The black dashed lines correspond to constant (homogeneous) initial conditions. All cross-plots have been colour-coded based on the distance from the edge of the crystal. Error bars are 1σ uncertainties from repeat measurements of San Carlos olivine secondary standards.

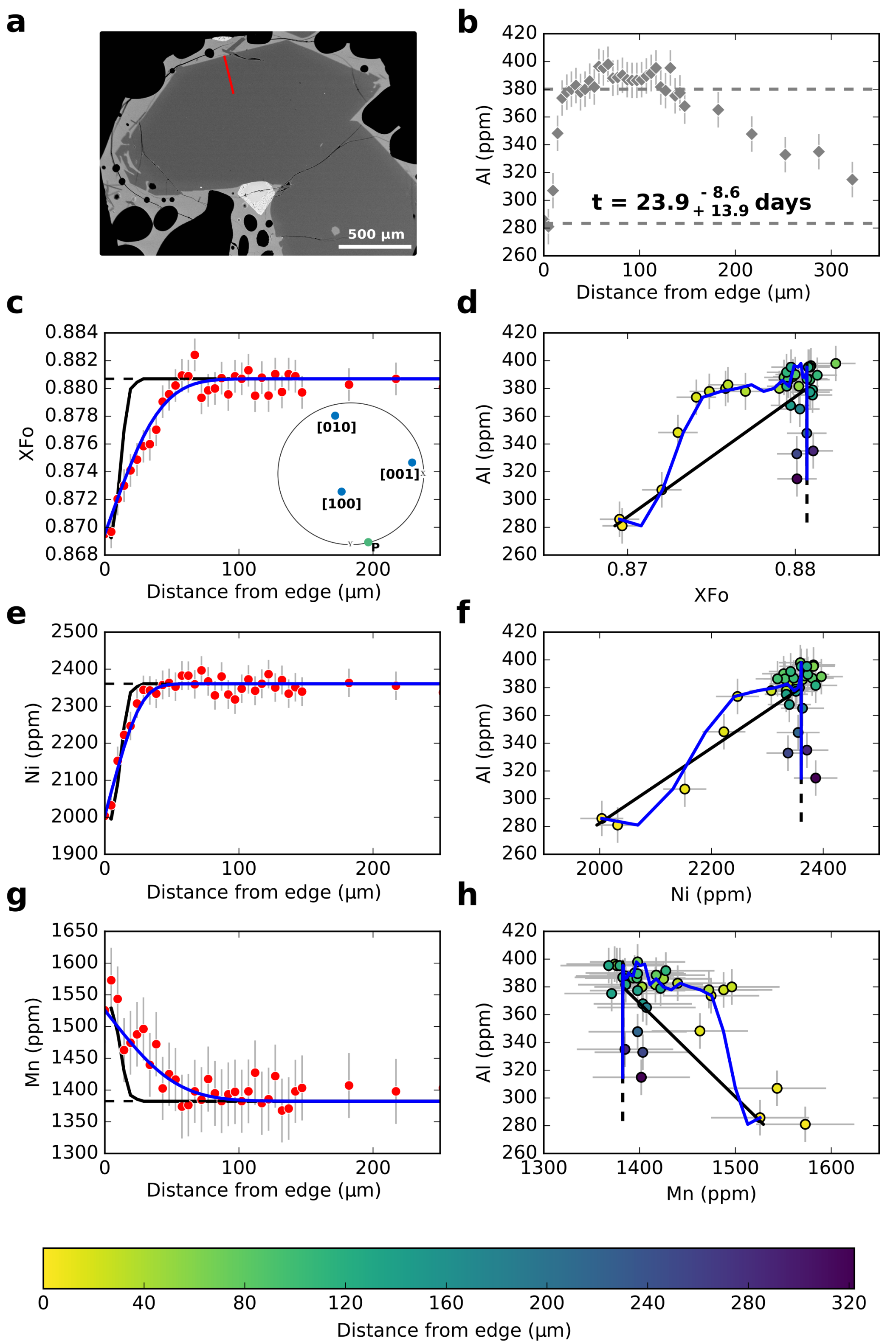

Supplementary Fig. 5: Data, initial conditions and model fits for sample BORG14_OL_C25_P1. Caption the same as Supplementary Fig. 4.

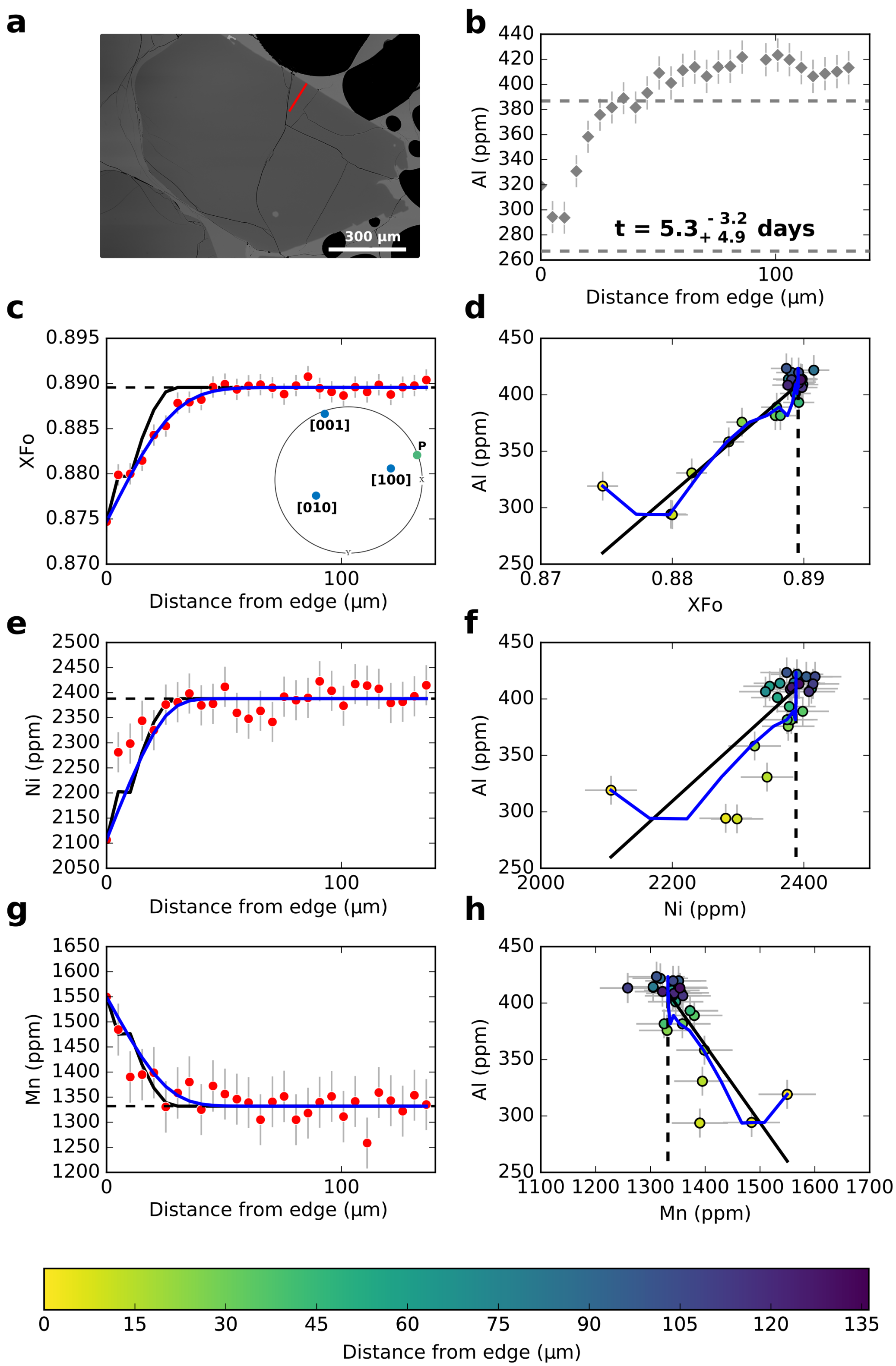

Supplementary Fig. 6: Data, initial conditions and model fits for sample BORG_NOD1_N2_C1_P1. Caption the same as Supplementary Fig. 4.

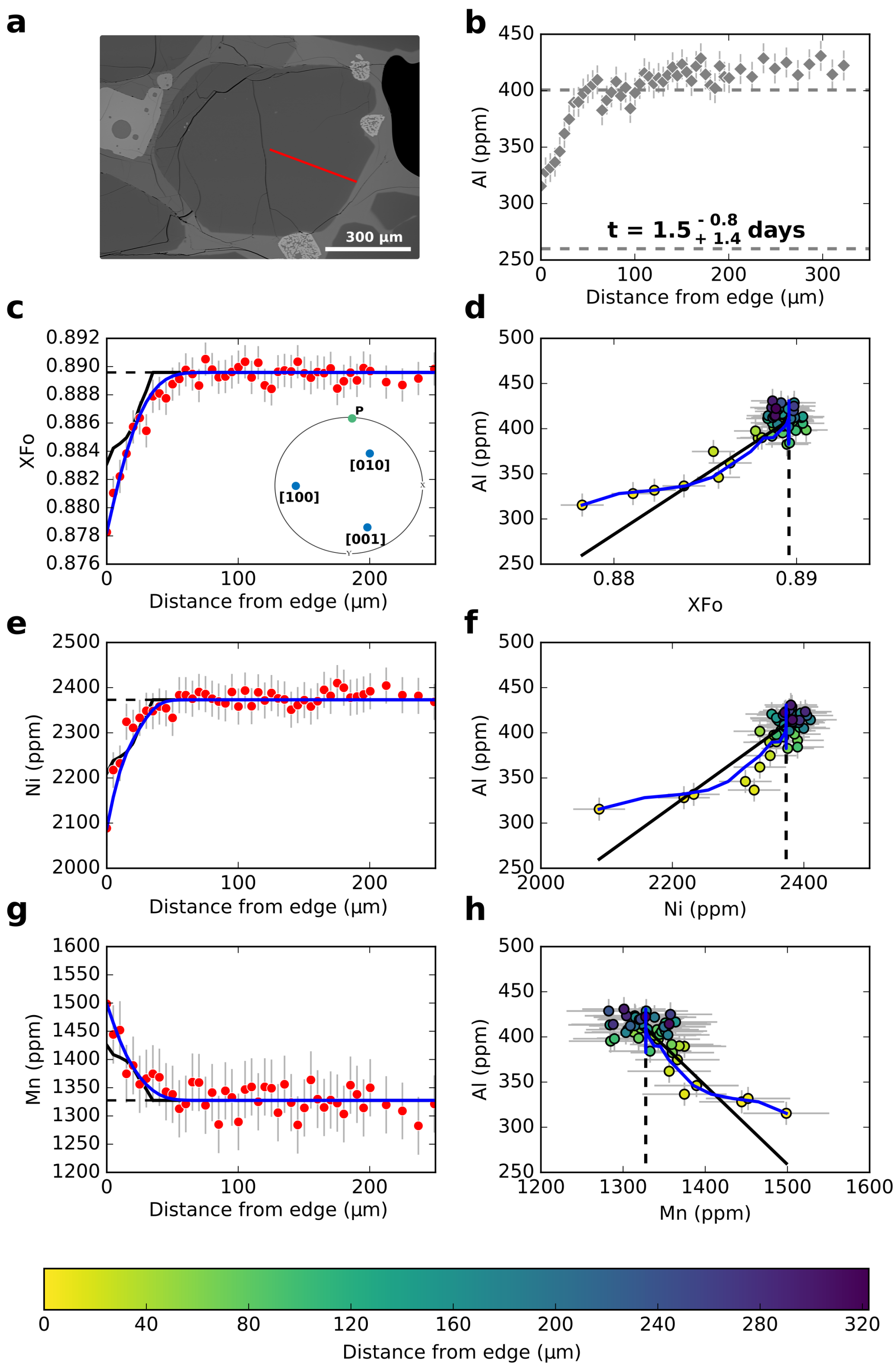

Supplementary Fig. 7: Data, initial conditions and model fits for sample BORG_NOD1_N3_C1_P2. Caption the same as Supplementary Fig. 4.

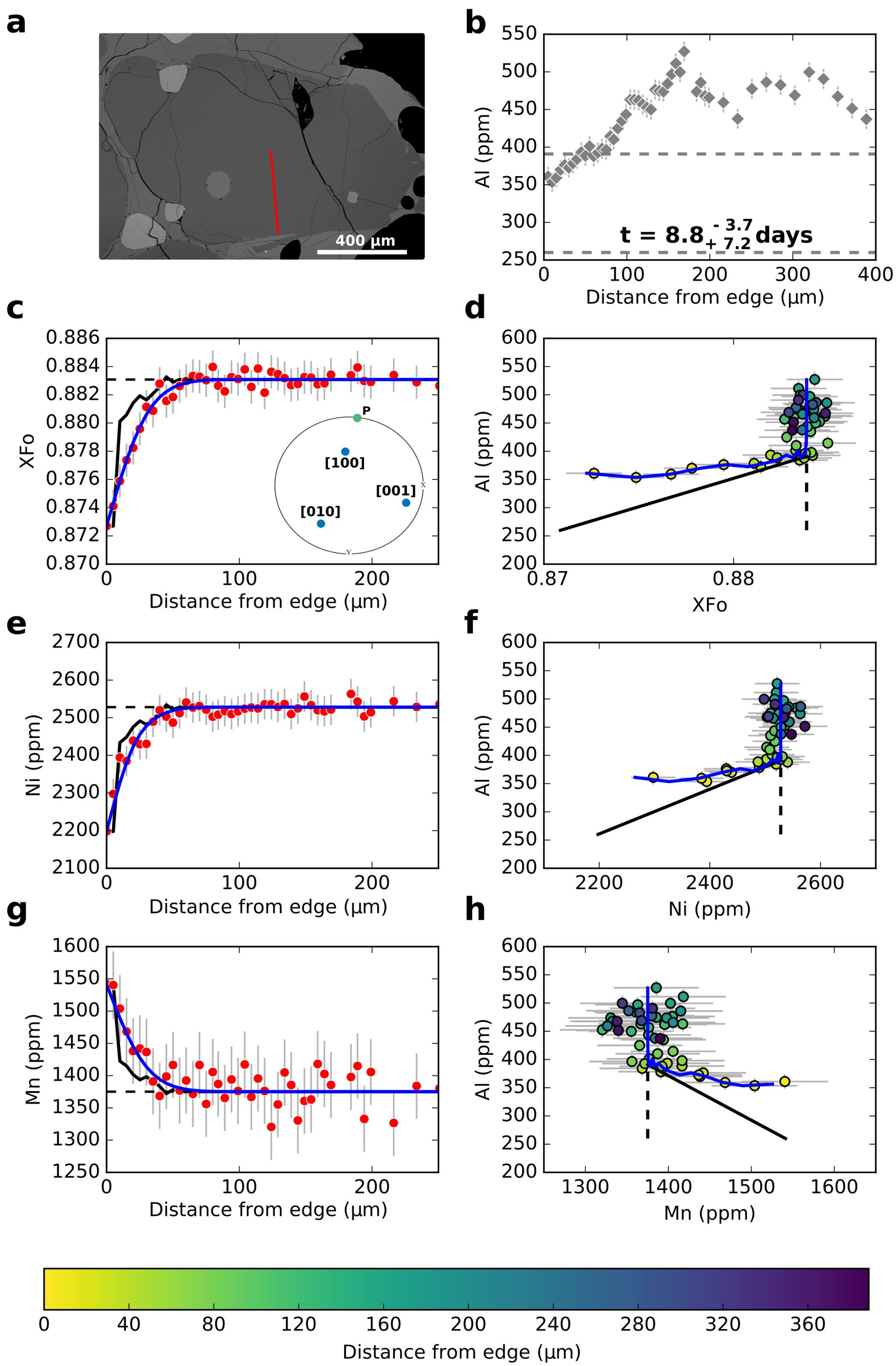

Supplementary Fig. 8: Data, initial conditions and model fits for sample BORG_NOD1_N5_C1_P1. Caption the same as Supplementary Fig. 4.

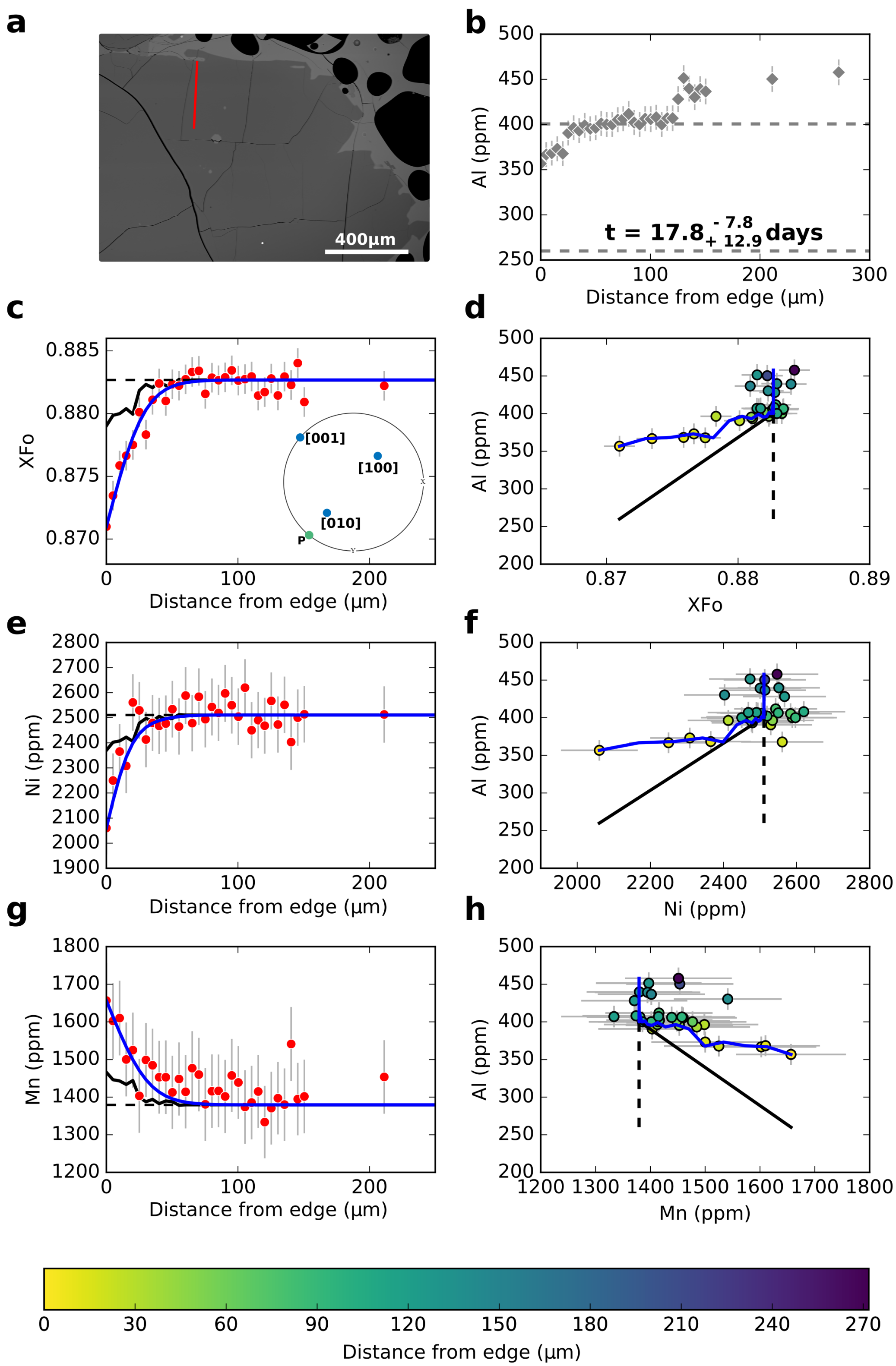

Supplementary Fig. 9: Data, initial conditions and model fits for sample BORG_NOD1_N5_C2_P1. Caption the same as Supplementary Fig. 4.

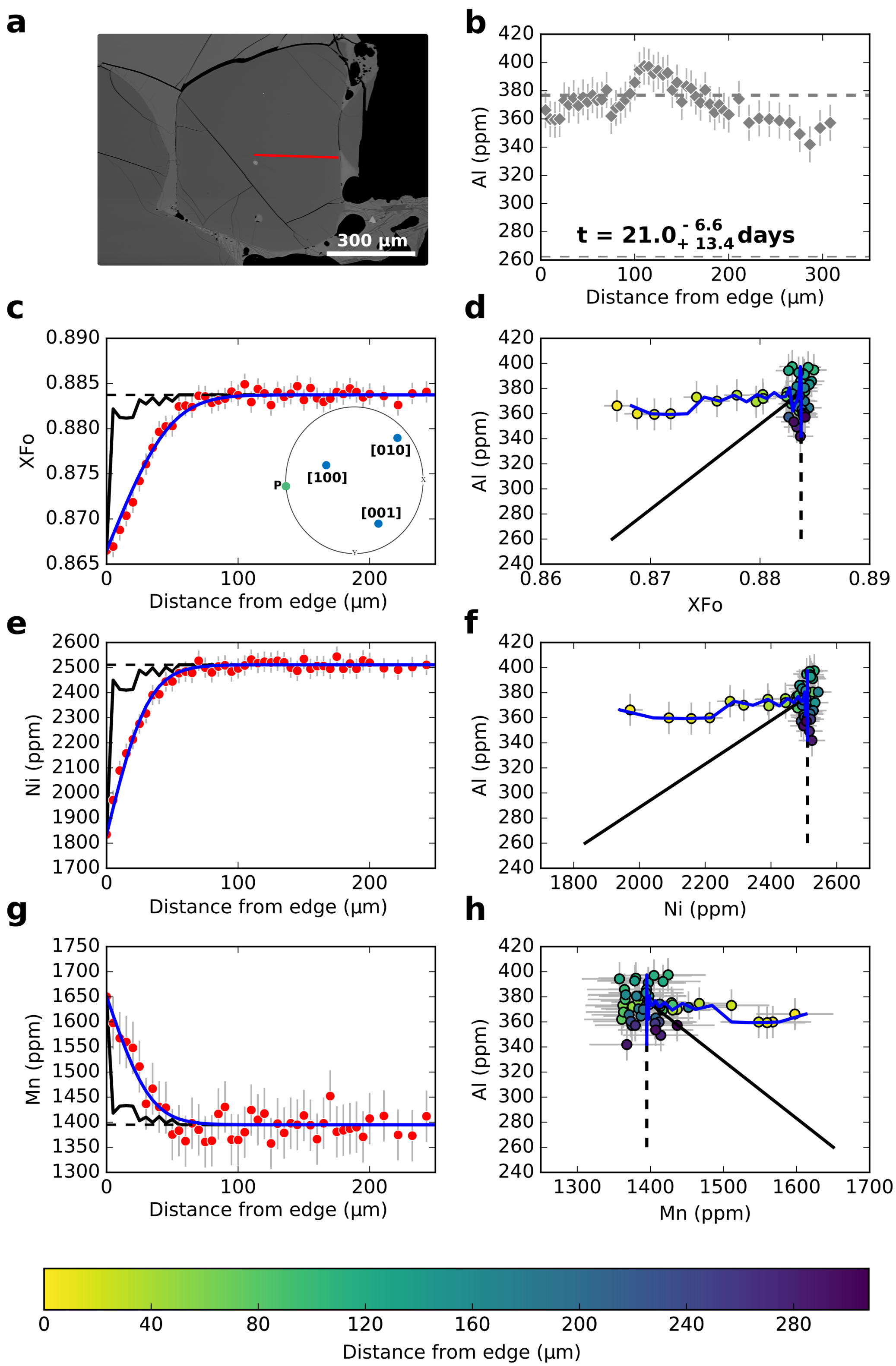

Supplementary Fig. 10: Data, initial conditions and model fits for sample BORG_NOD1_N6_C2_P1. Caption the same as Supplementary Fig. 4.

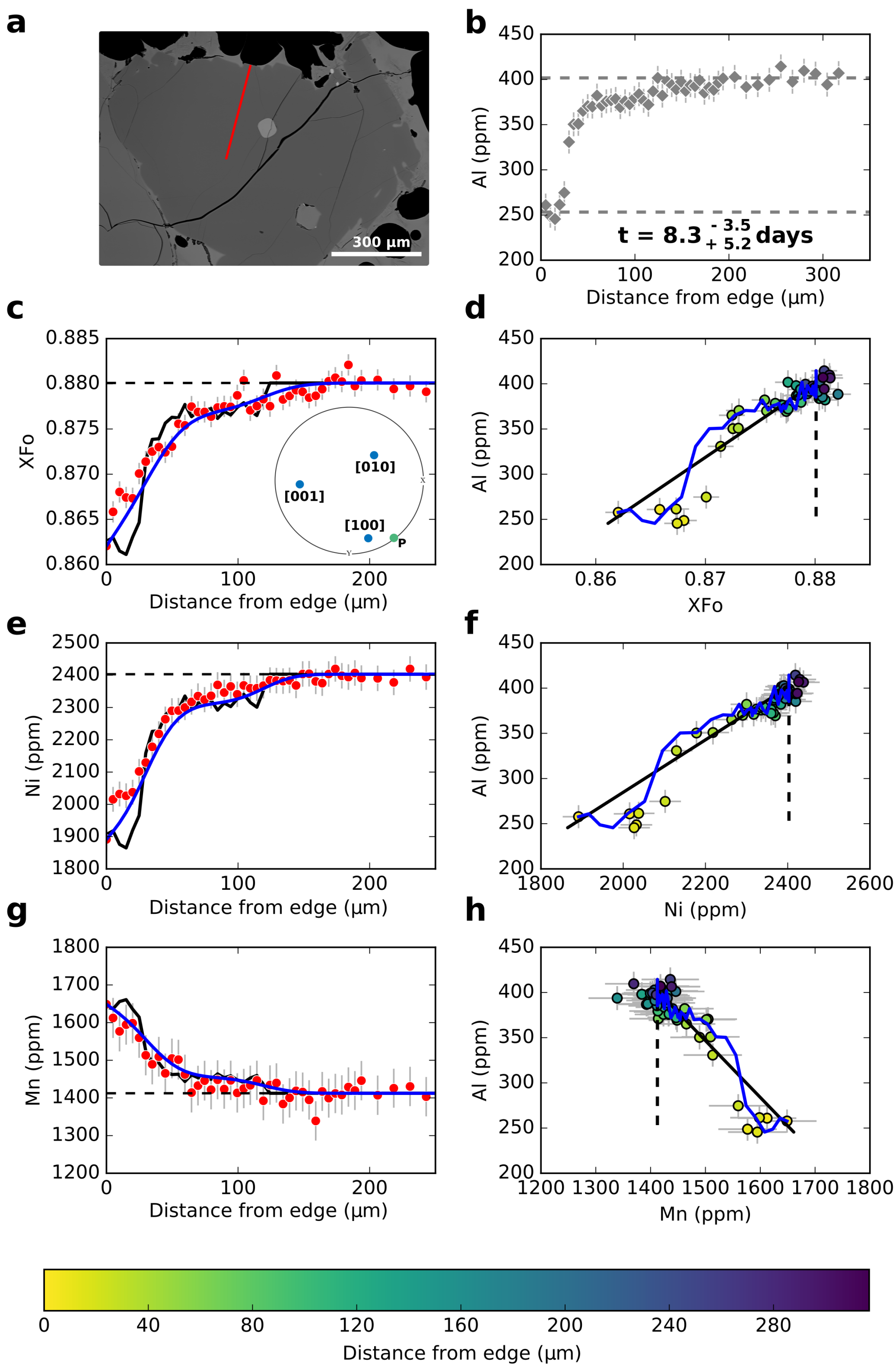

Supplementary Fig. 11: Data, initial conditions and model fits for sample BORG_NOD2_N1_C3_P2. Caption the same as Supplementary Fig. 4.

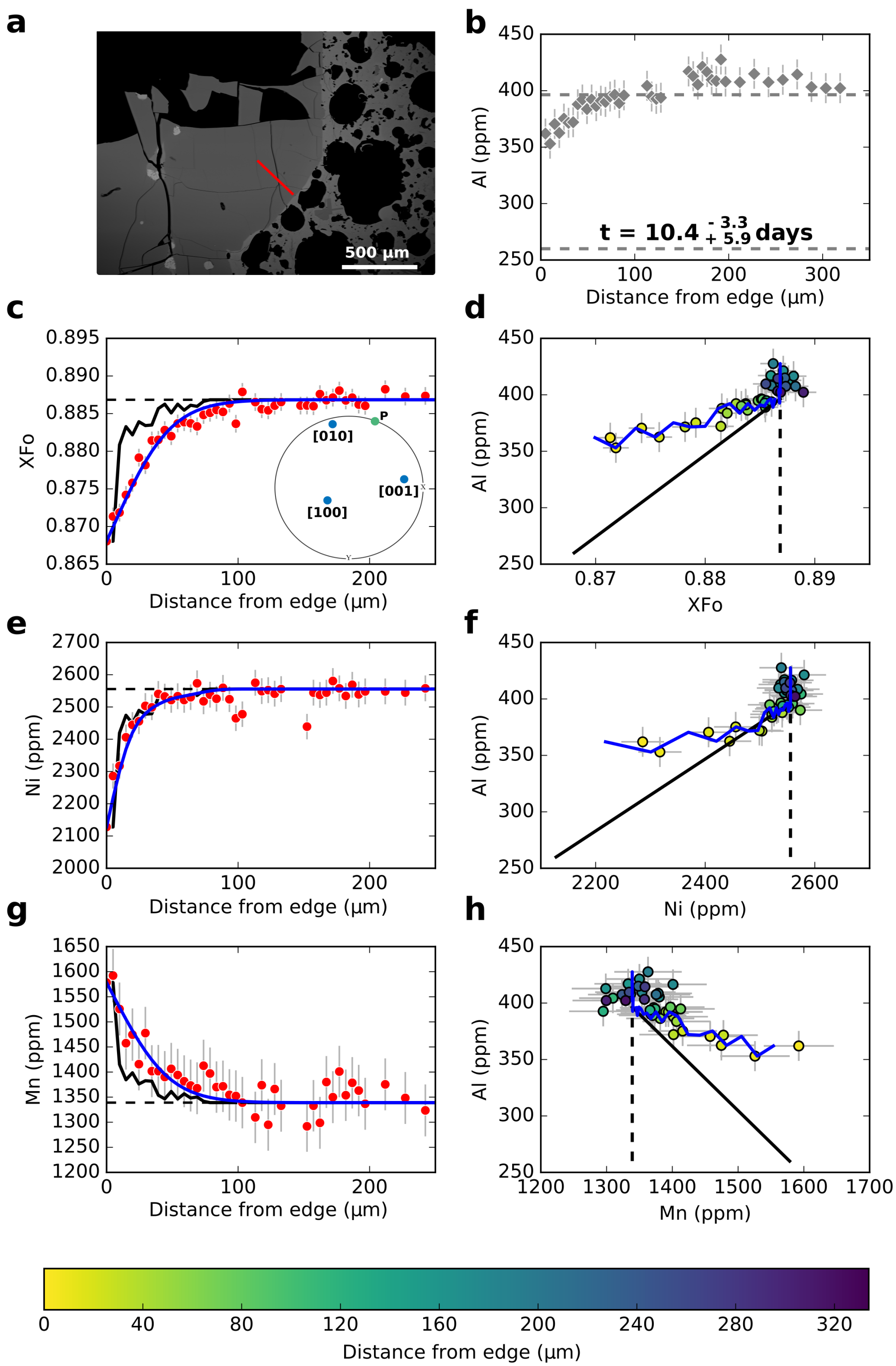

Supplementary Fig. 12: Data, initial conditions and model fits for sample BORG_NOD2_N2_C4_P2. Caption the same as Supplementary Fig. 4.

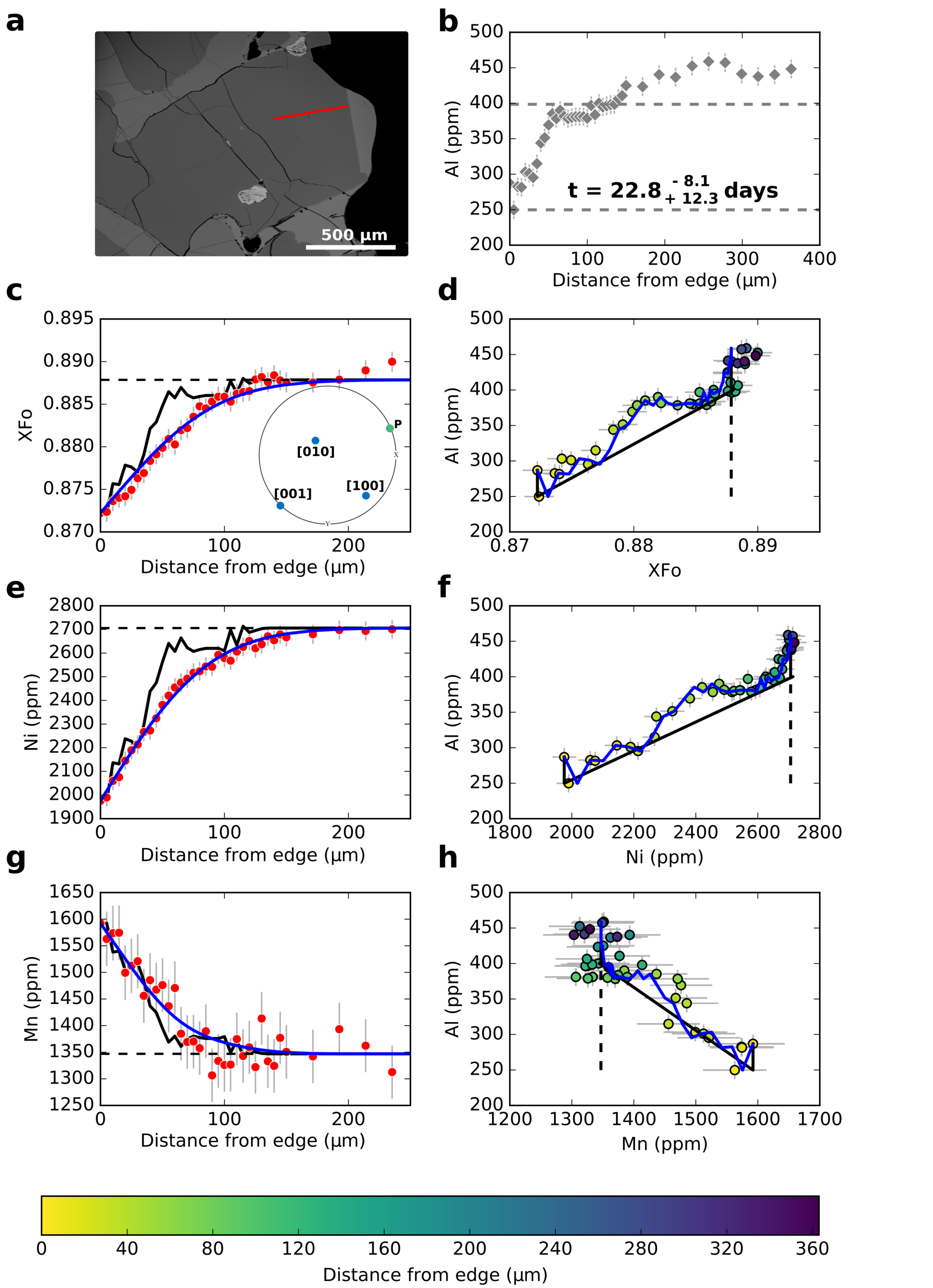

Supplementary Fig. 13: Data, initial conditions and model fits for sample BORG_NOD2_N3_C2_P1. Caption the same as Supplementary Fig. 4.

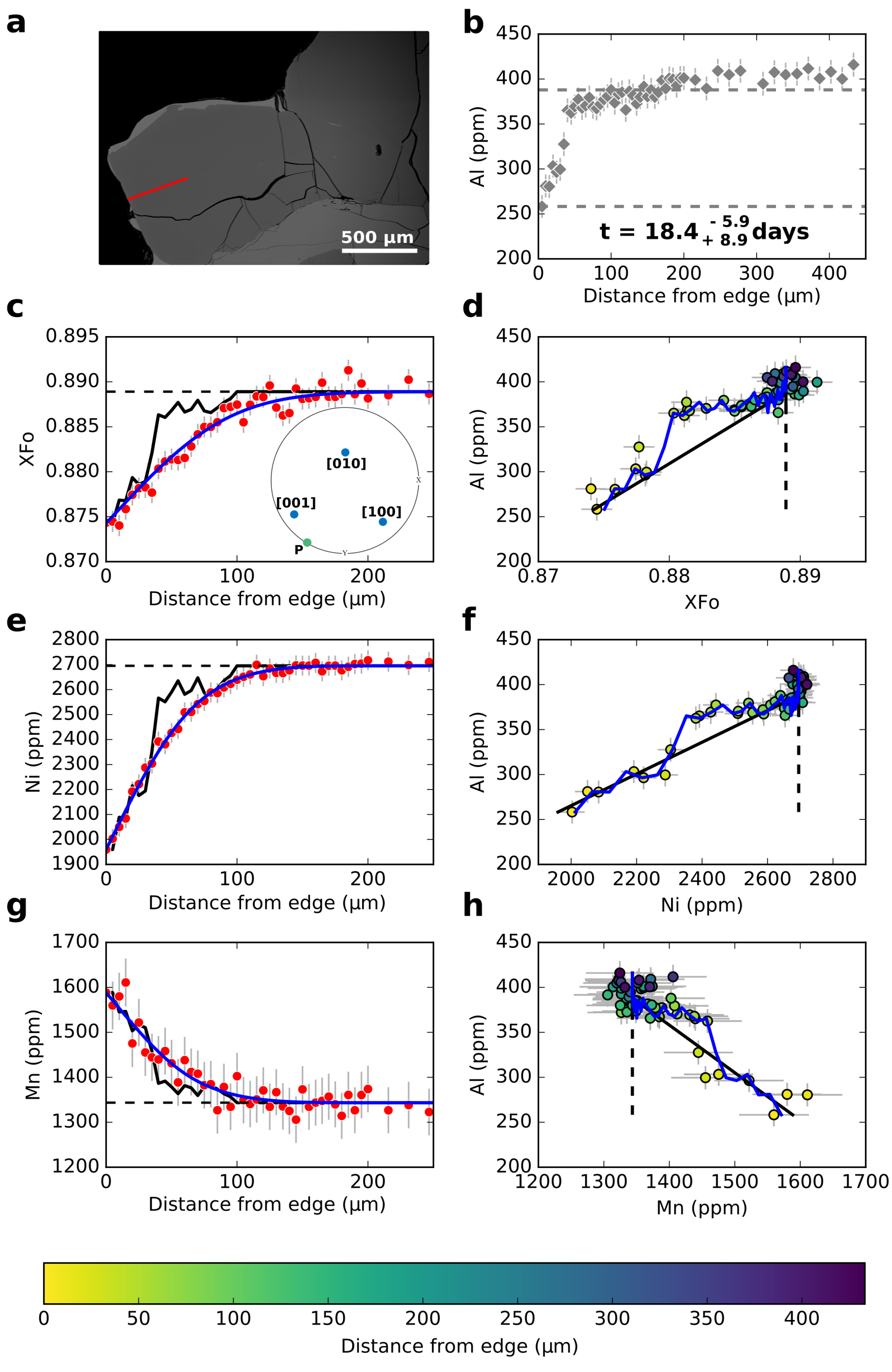

Supplementary Fig. 14: Data, initial conditions and model fits for sample BORG_NOD2_N3_C6_P2. Caption the same as Supplementary Fig. 4.

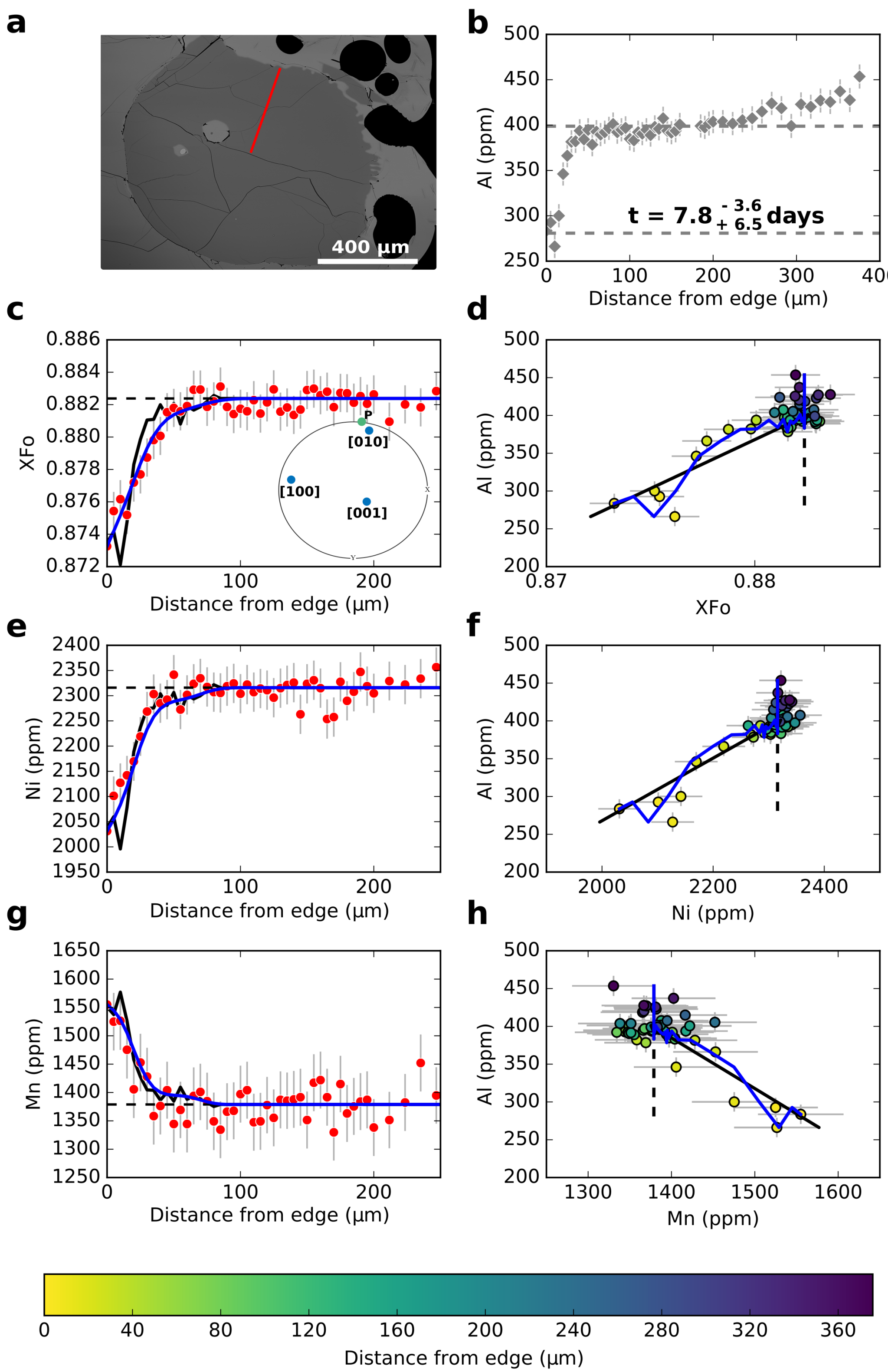

Supplementary Fig. 15: Data, initial conditions and model fits for sample BORG_NOD3_N1_C1_P2. Caption the same as Supplementary Fig. 4.

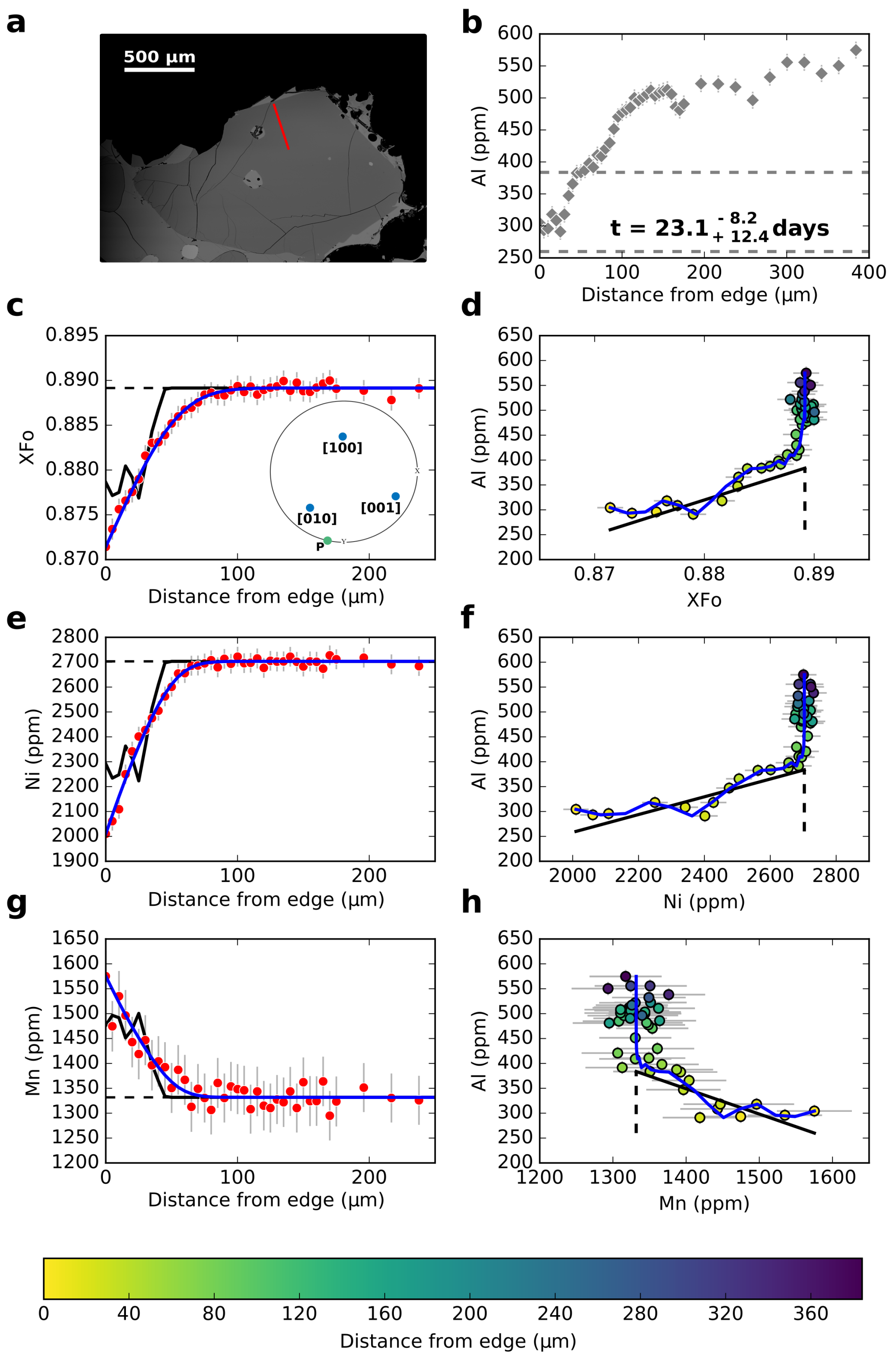

Supplementary Fig. 16: Data, initial conditions and model fits for sample BORG_NOD3_N2_C1_P2. Caption the same as Supplementary Fig. 4.

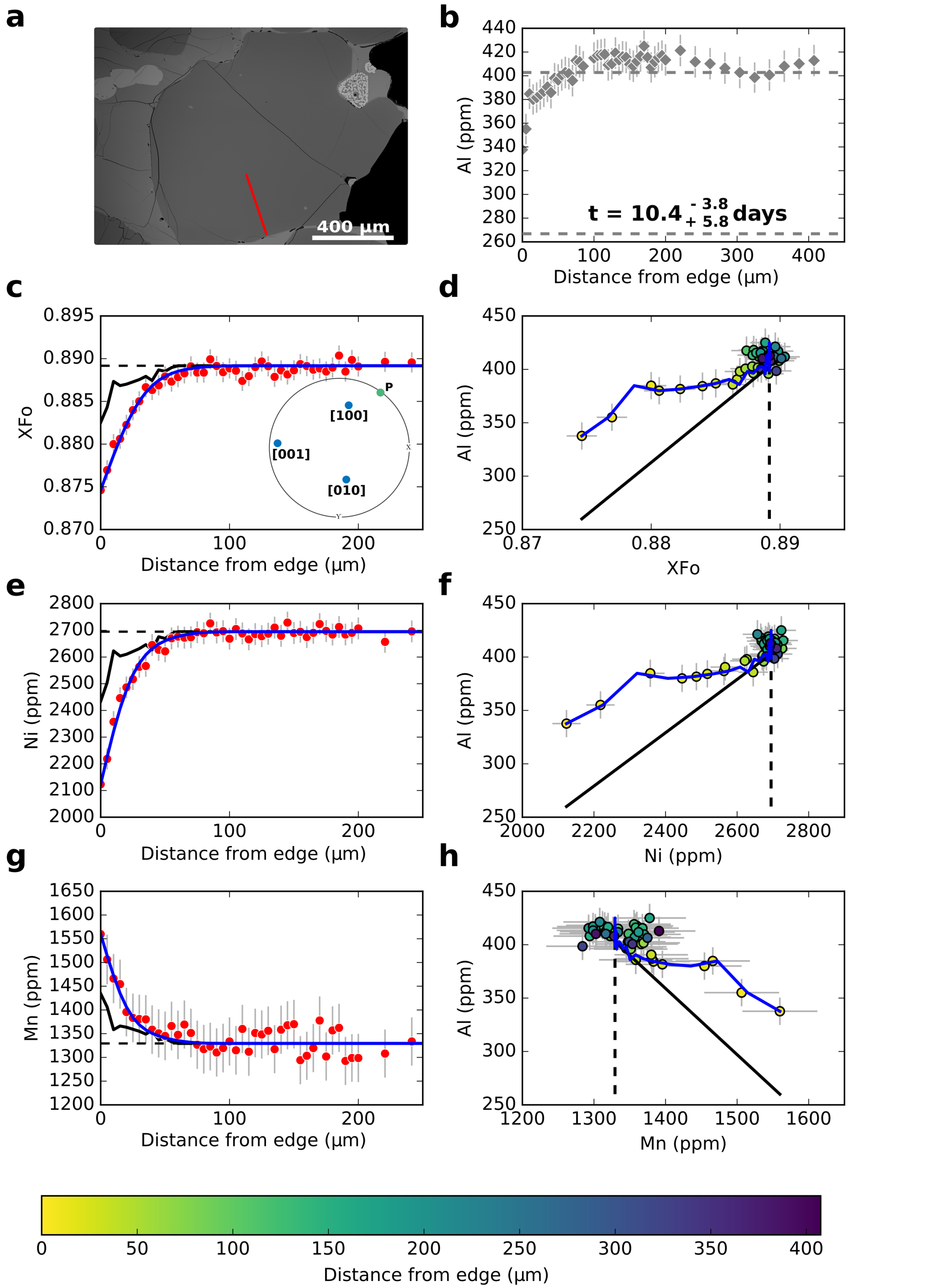

Supplementary Fig. 17: Data, initial conditions and model fits for sample BORG_NOD3_N2_C2_P2. Caption the same as Supplementary Fig. 4.

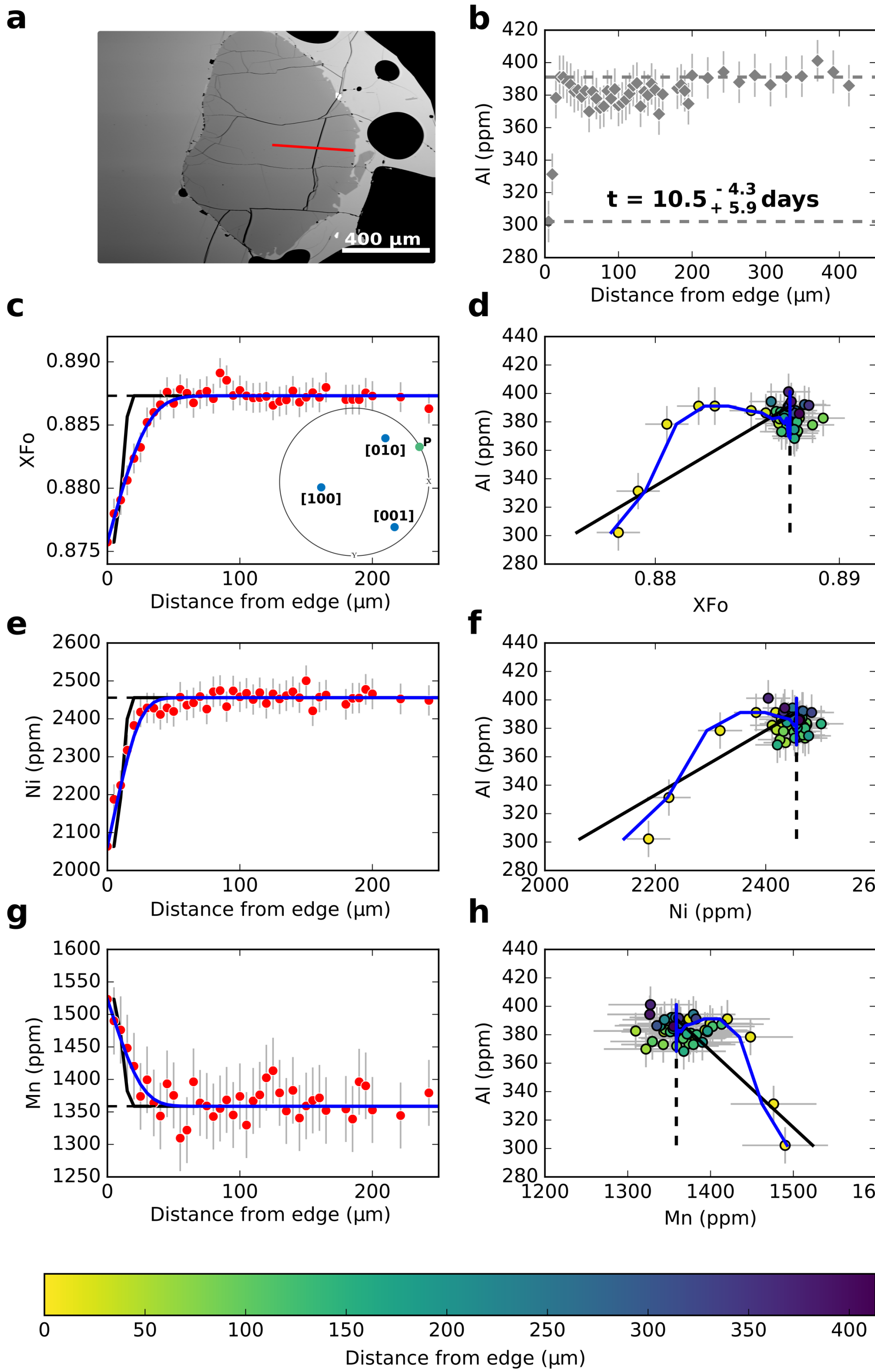

Supplementary Fig. 18: Data, initial conditions and model fits for sample BORG_NOD3_N3_C1_P2. Caption the same as Supplementary Fig. 4.

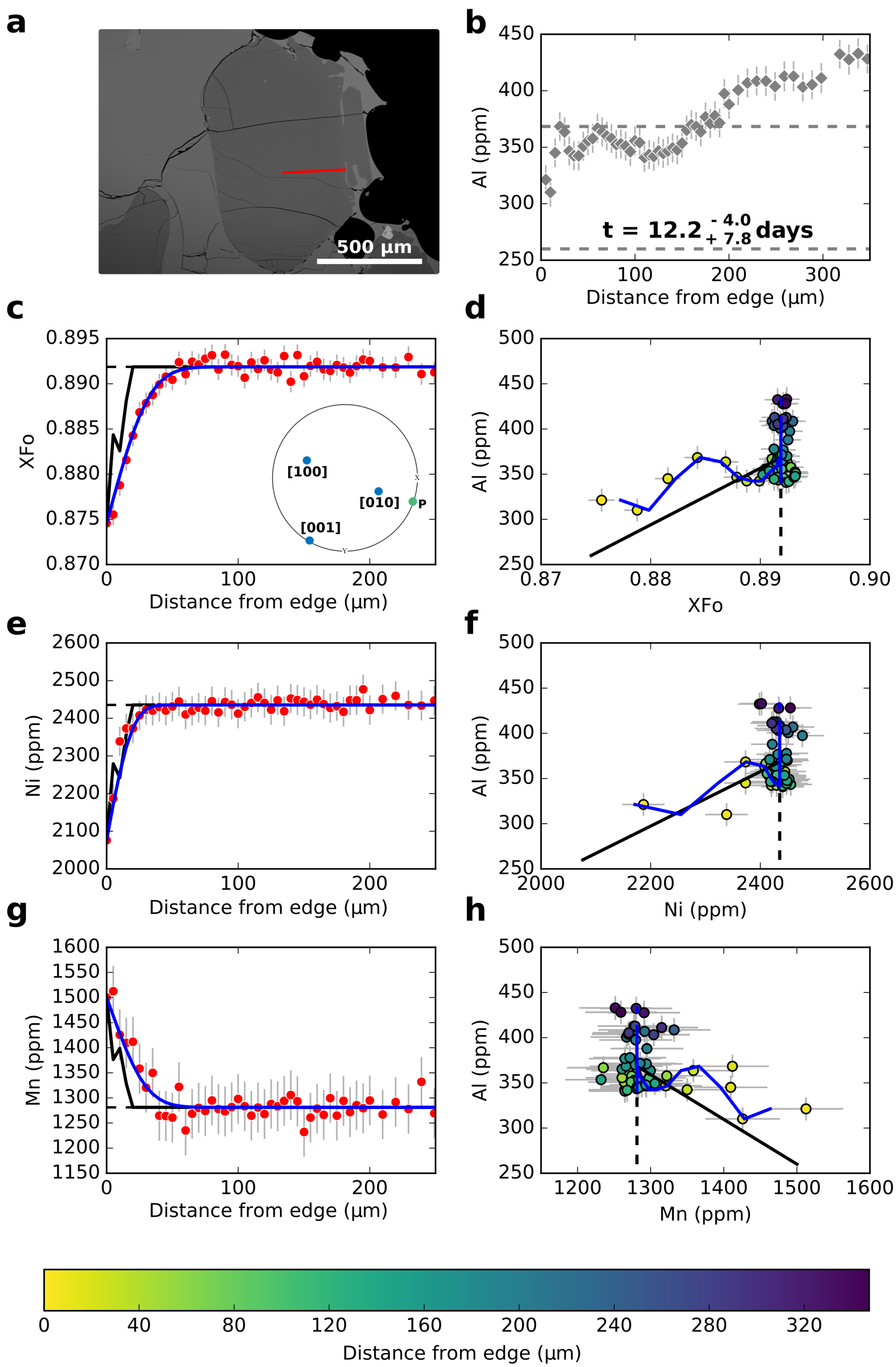

Supplementary Fig. 19: Data, initial conditions and model fits for sample BORG_NOD3_N4_C1_P1. Caption the same as Supplementary Fig. 4.

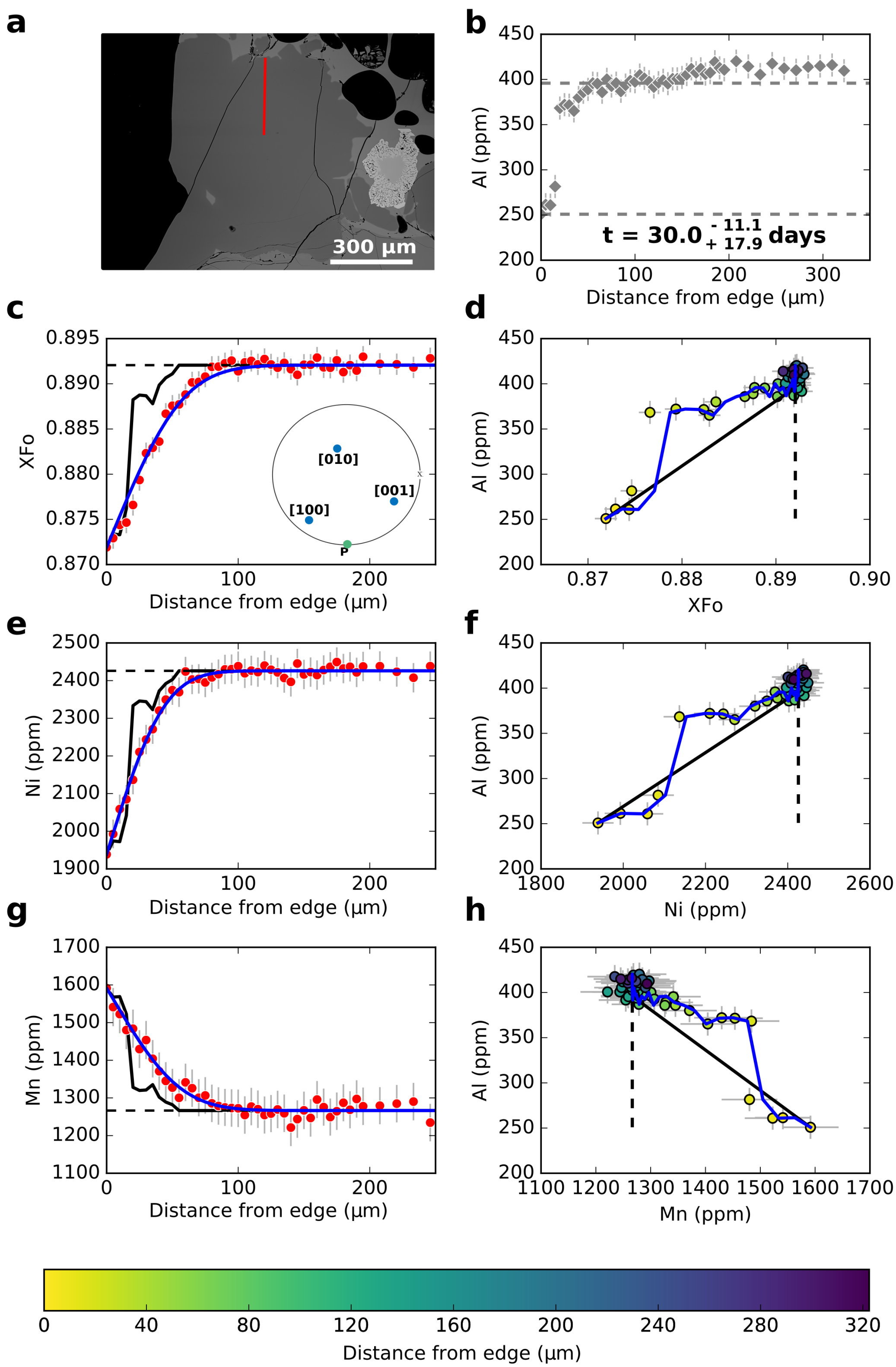

Supplementary Fig. 20: Data, initial conditions and model fits for sample BORG_NOD3_N4_C3_P2. Caption the same as Supplementary Fig. 4.

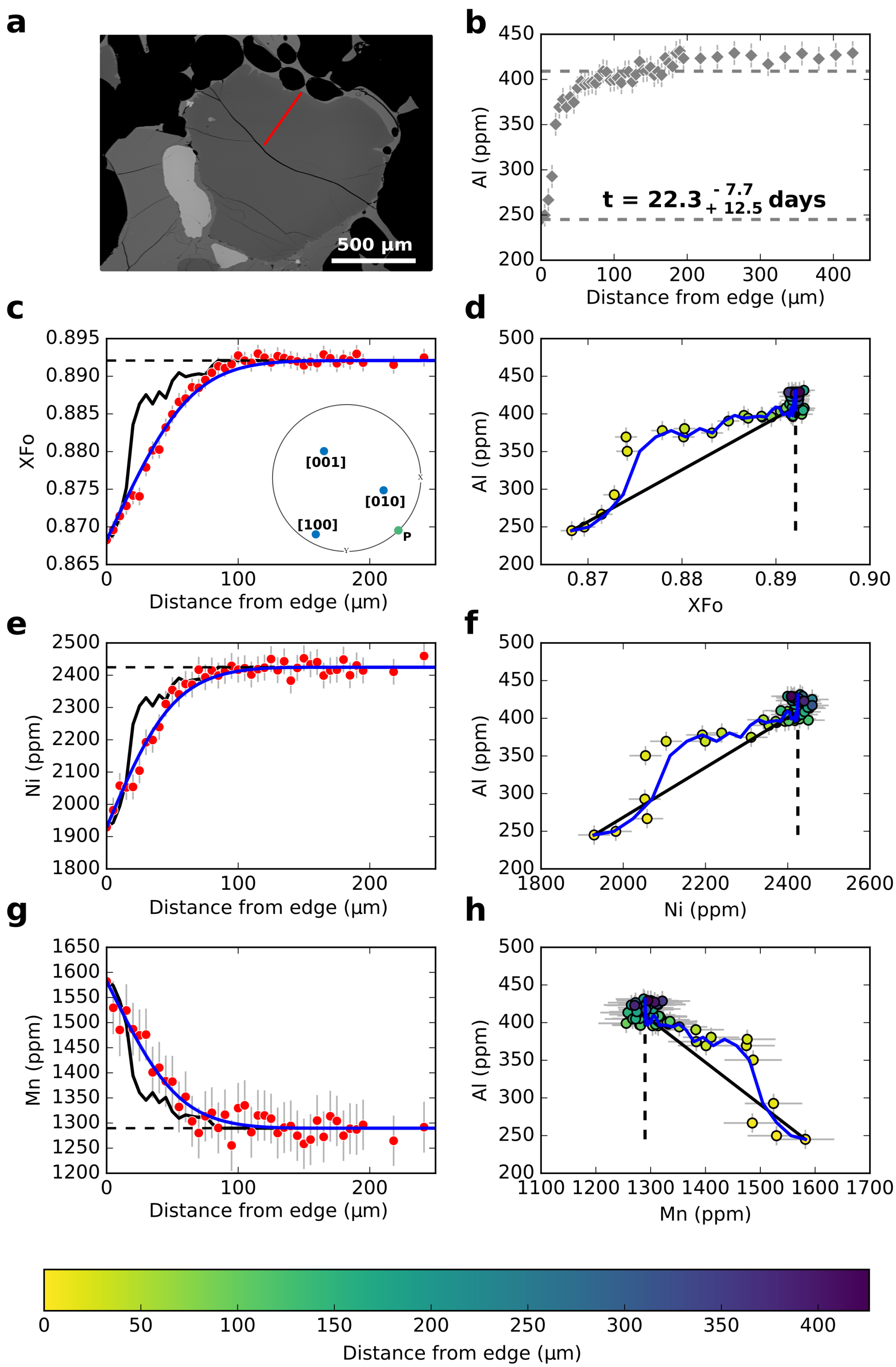

Supplementary Fig. 21: Data, initial conditions and model fits for sample BORG_NOD3_N7_C1_P2. Caption the same as Supplementary Fig. 4.

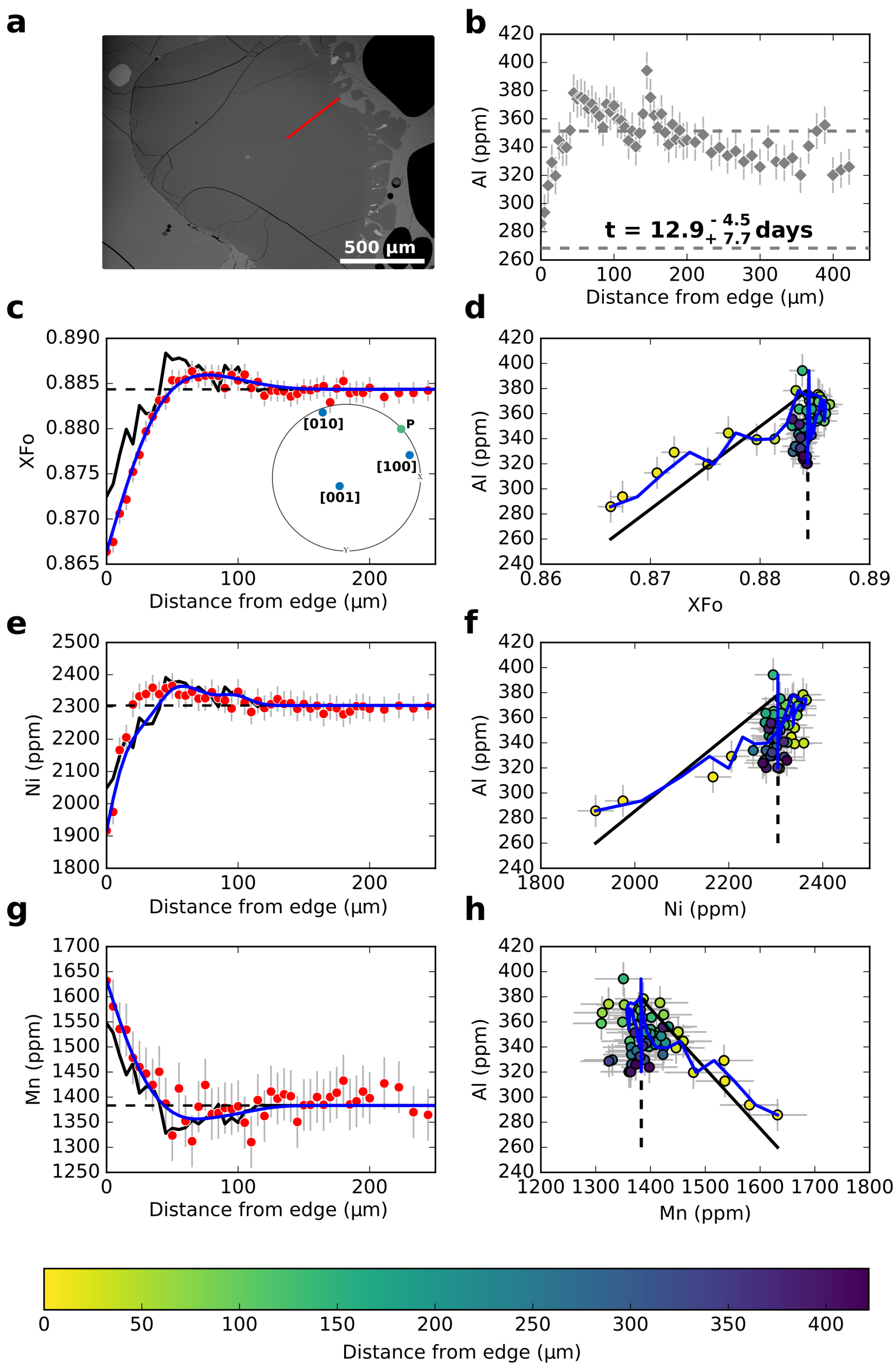

Supplementary Fig. 22: Data, initial conditions and model fits for sample BORG_NOD5_N1_C1_P2. Caption the same as Supplementary Fig. 4.

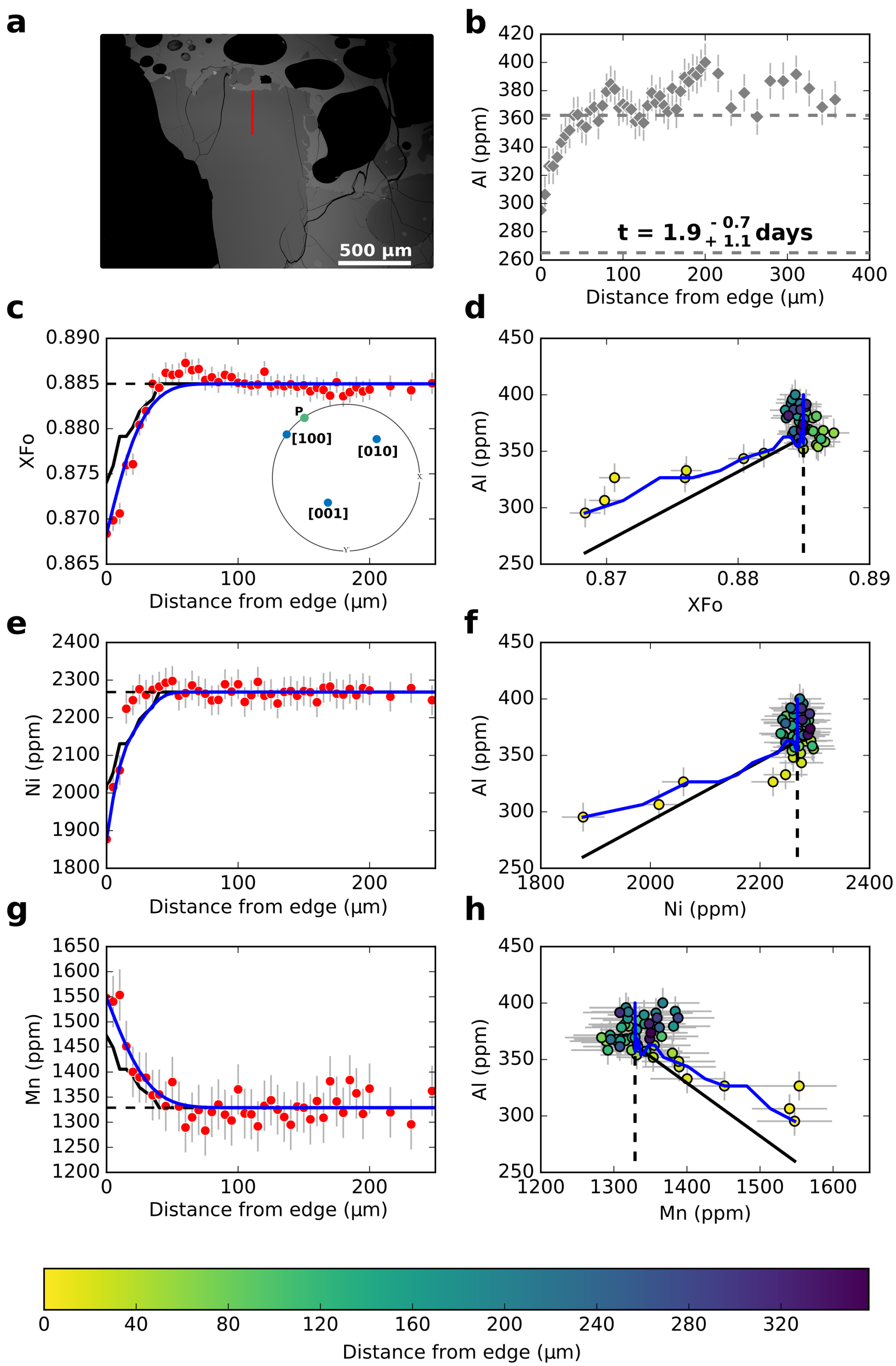

Supplementary Fig. 23: Data, initial conditions and model fits for sample BORG_NOD5_N1_C2_P2. Caption the same as Supplementary Fig. 4.

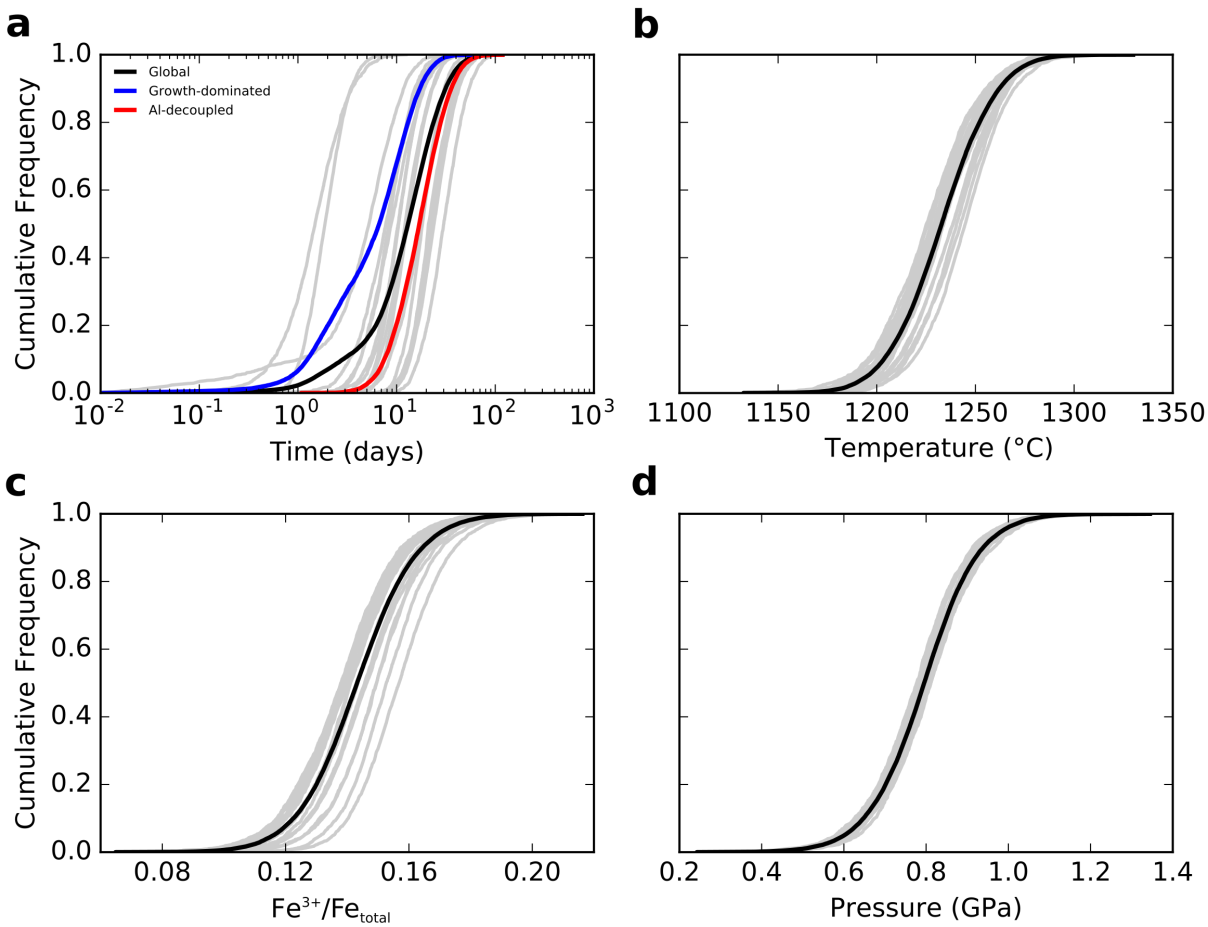

Supplementary Fig. 24: Cumulative frequency distributions for parameters estimated from the Bayesian Inversion using Al-based initial conditions. a, time (days); **b,** temperature (°C), **c,** Fe^{3+}/Fe_{total}; **d,** pressure (GPa).

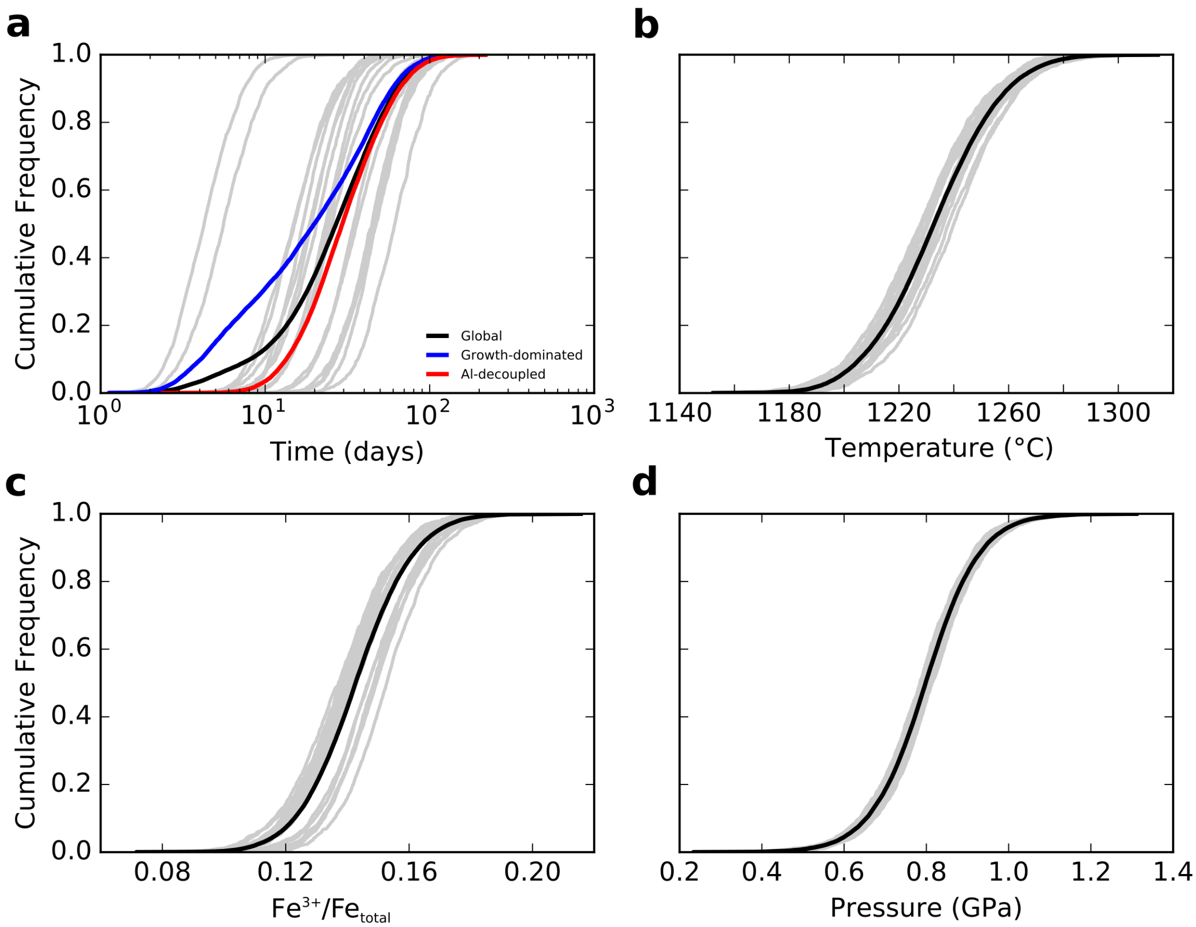

Supplementary Fig. 25: Cumulative frequency distributions for parameters estimated from the Bayesian Inversion using constant initial conditions. a, time (days); **b,** temperature (°C), **c,** Fe^{3+}/Fe_{total}; **d,** pressure (GPa).

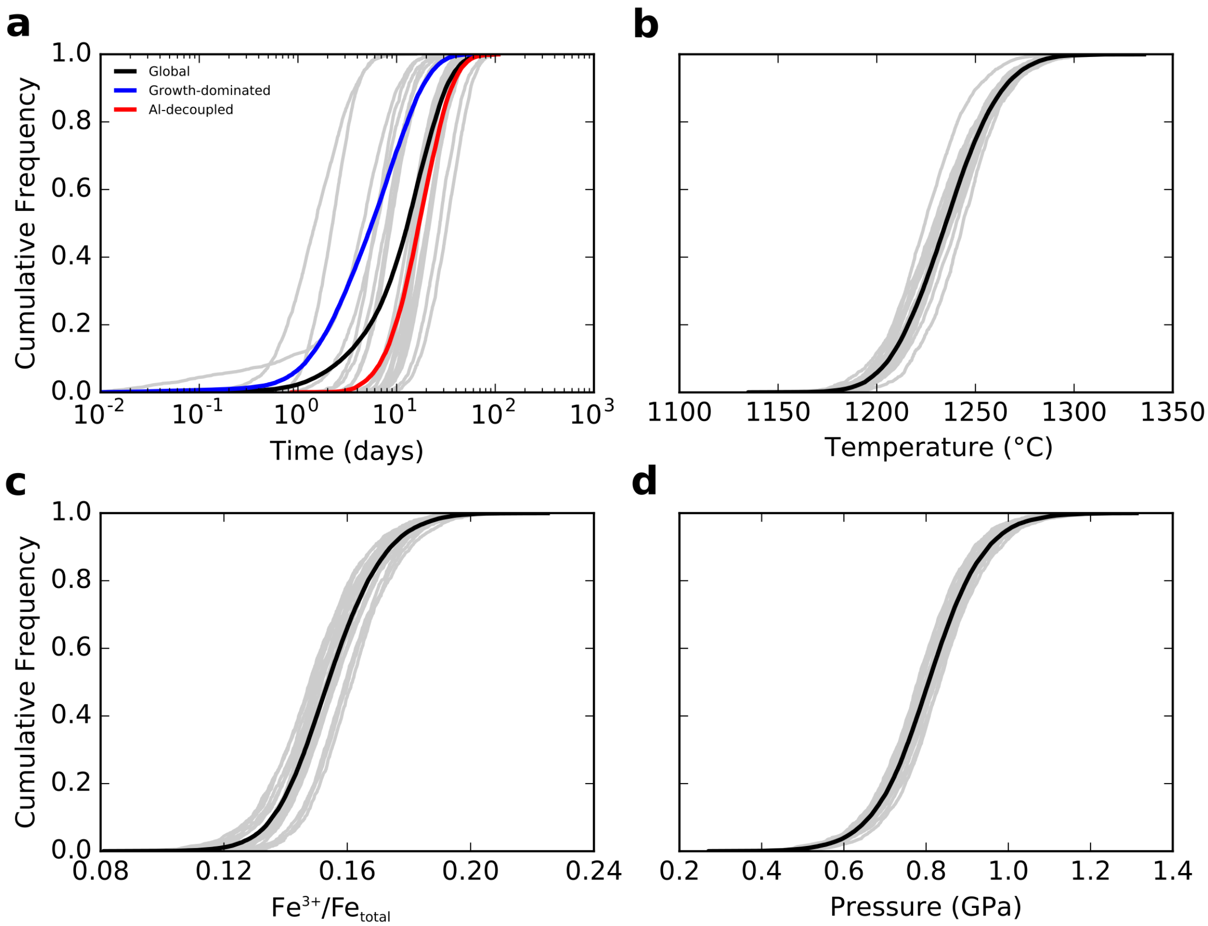

Supplementary Fig. 26: Cumulative frequency distributions for parameters estimated from the Bayesian Inversion using Al-based initial conditions and $a_{\mathrm{SiO_2}}$ dependent diffusion equations. a, time (days); **b,** temperature (°C), **c,** Fe^{3+}/Fe_{total}; **d,** pressure (GPa).

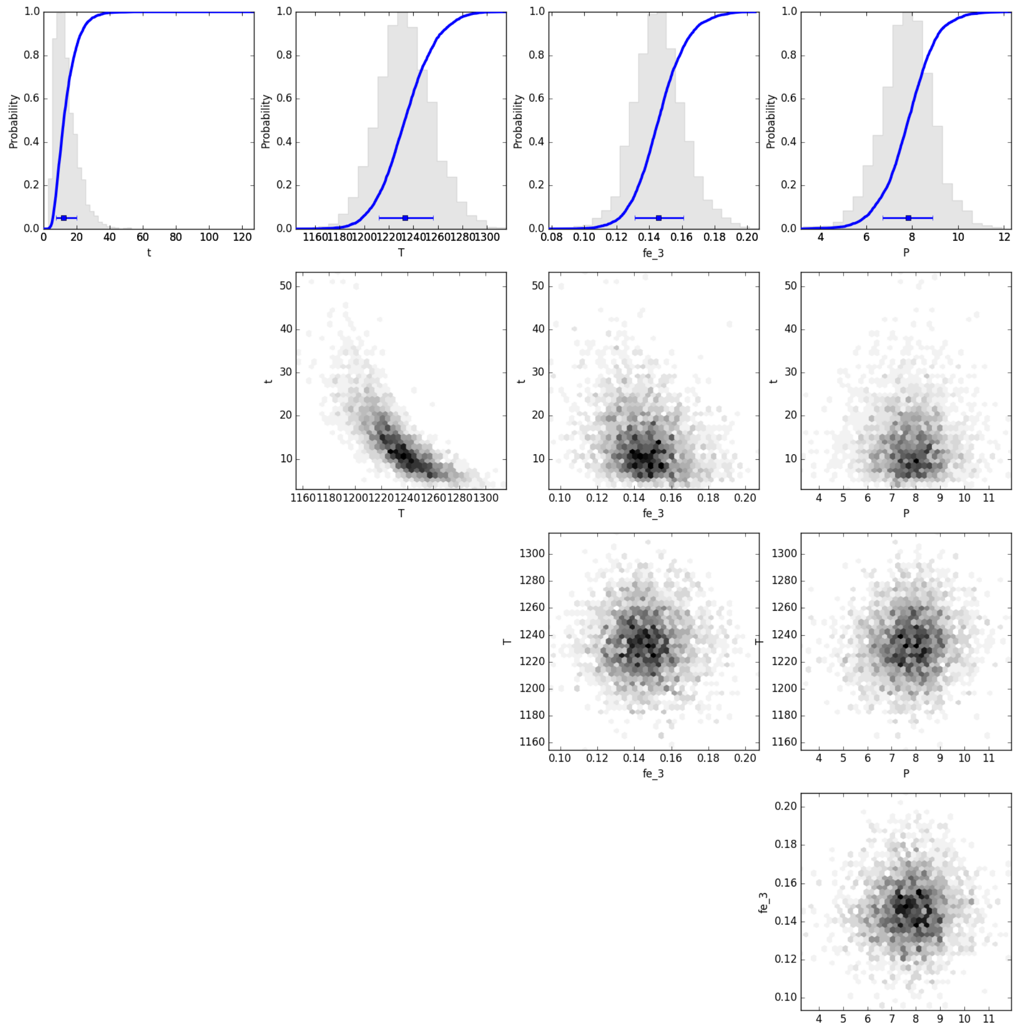

Supplementary Fig. 27: Bayesian inversion results for sample BORG14_OL_C2_P1. Marginal plot showing the posterior distributions of the Nested Sampling Bayesian Inversion for the main intensive parameters: t is time (days), T is temperature (°C), fe_3 is ferric iron content of the melt and P is pressure (kbar). The top row shows histograms (grey bars) and probablility density functions (blue curves) of the afformentioned intensive parameters. The blue bar shows the median result and 1σ standard deviation. The bottom three rows are density plots that show the trade offs between the different initensive parameters. These results are for models that used the Al-based (growth-controlled) initial conditions and $a_{\mathrm{SiO_2}}$ independent olivine diffusion equations.

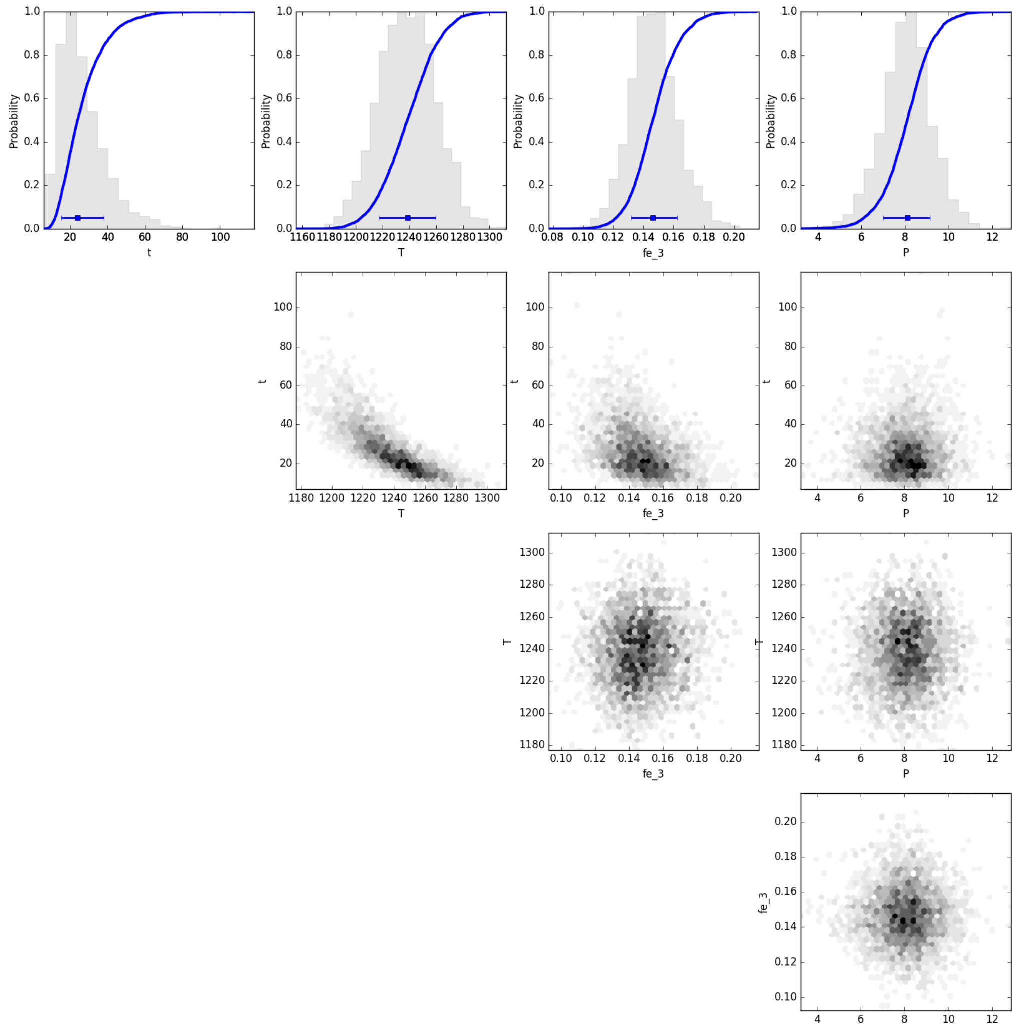

Supplementary Fig. 28: Bayesian inversion results for sample BORG14_OL_C25_P1. Marginal plot showing the posterior distributions of the Nested Sampling Bayesian Inversion for the main intensive parameters: t is time (days), T is temperature (°C), fe_3 is ferric iron content of the melt and P is pressure (kbar). The top row shows histograms (grey bars) and probablility density functions (blue curves) of the afformentioned intensive parameters. The blue bar shows the median result and 1σ standard deviation. The bottom three rows are density plots that show the trade offs between the different initensive parameters. These results are for models that used the Al-based (growth-controlled) initial conditions and $a_{\mathrm{SiO_2}}$ independent olivine diffusion equations.

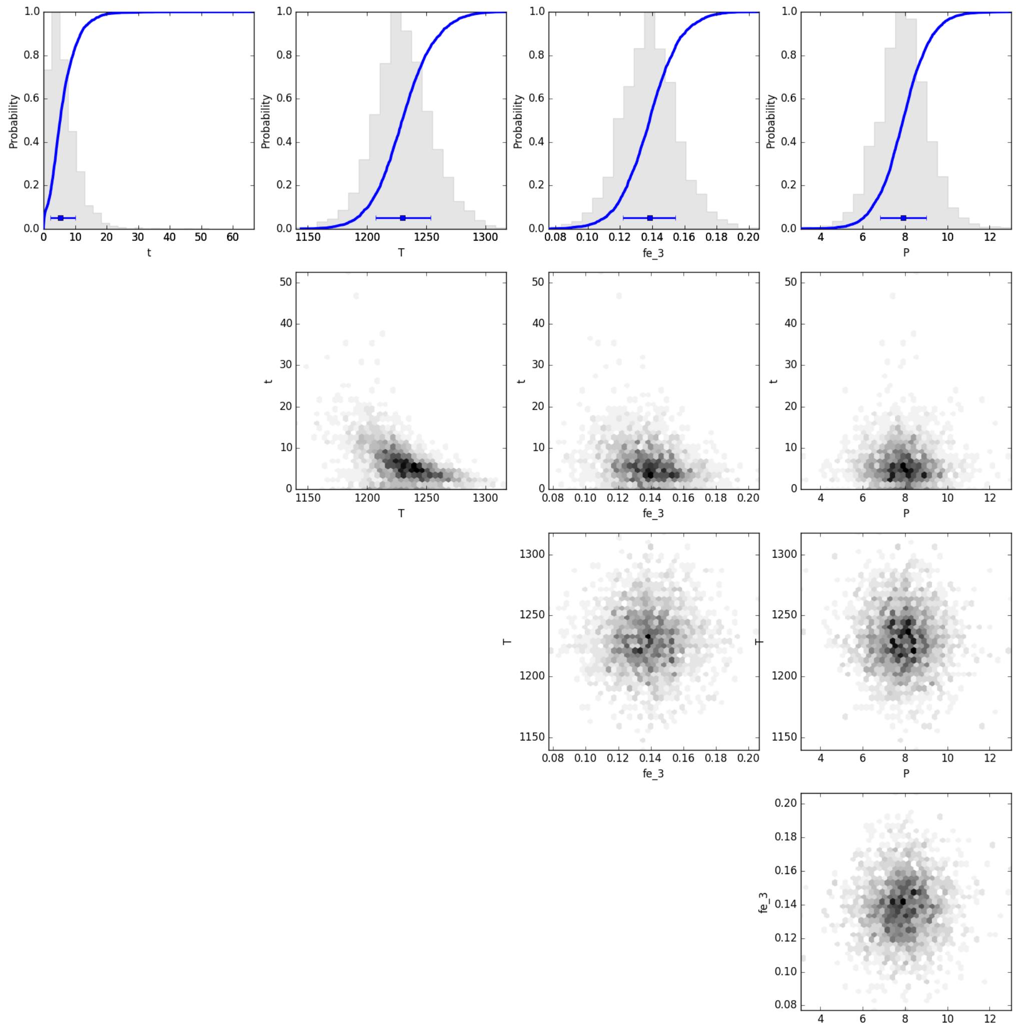

Supplementary Fig. 29: Bayesian inversion results for sample BORG_NOD1_N2_C1_P1. Marginal plot showing the posterior distributions of the Nested Sampling Bayesian Inversion for the main intensive parameters: t is time (days), T is temperature (°C), fe_3 is ferric iron content of the melt and P is pressure (kbar). The top row shows histograms (grey bars) and probablility density functions (blue curves) of the afformentioned intensive parameters. The blue bar shows the median result and 1σ standard deviation. The bottom three rows are density plots that show the trade offs between the different initensive parameters. These results are for models that used the Al-based (growth-controlled) initial conditions and $a_{\mathrm{SiO_2}}$ independent olivine diffusion equations.

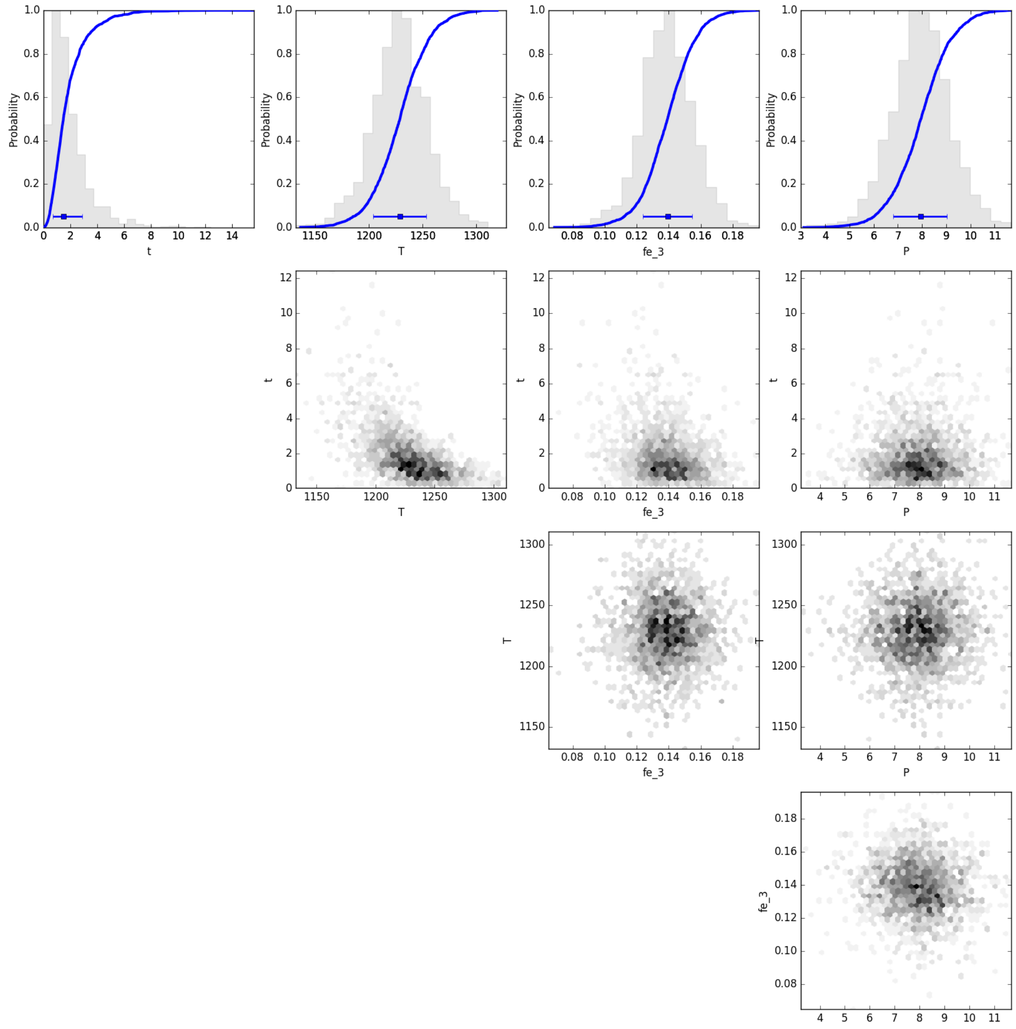

Supplementary Fig. 30: Bayesian inversion results for sample BORG_NOD1_N3_C1_P2. Marginal plot showing the posterior distributions of the Nested Sampling Bayesian Inversion for the main intensive parameters: t is time (days), T is temperature (°C), fe_3 is ferric iron content of the melt and P is pressure (kbar). The top row shows histograms (grey bars) and probablility density functions (blue curves) of the afformentioned intensive parameters. The blue bar shows the median result and 1σ standard deviation. The bottom three rows are density plots that show the trade offs between the different initensive parameters. These results are for models that used the Al-based (growth-controlled) initial conditions and $a_{\mathrm{SiO_2}}$ independent olivine diffusion equations.

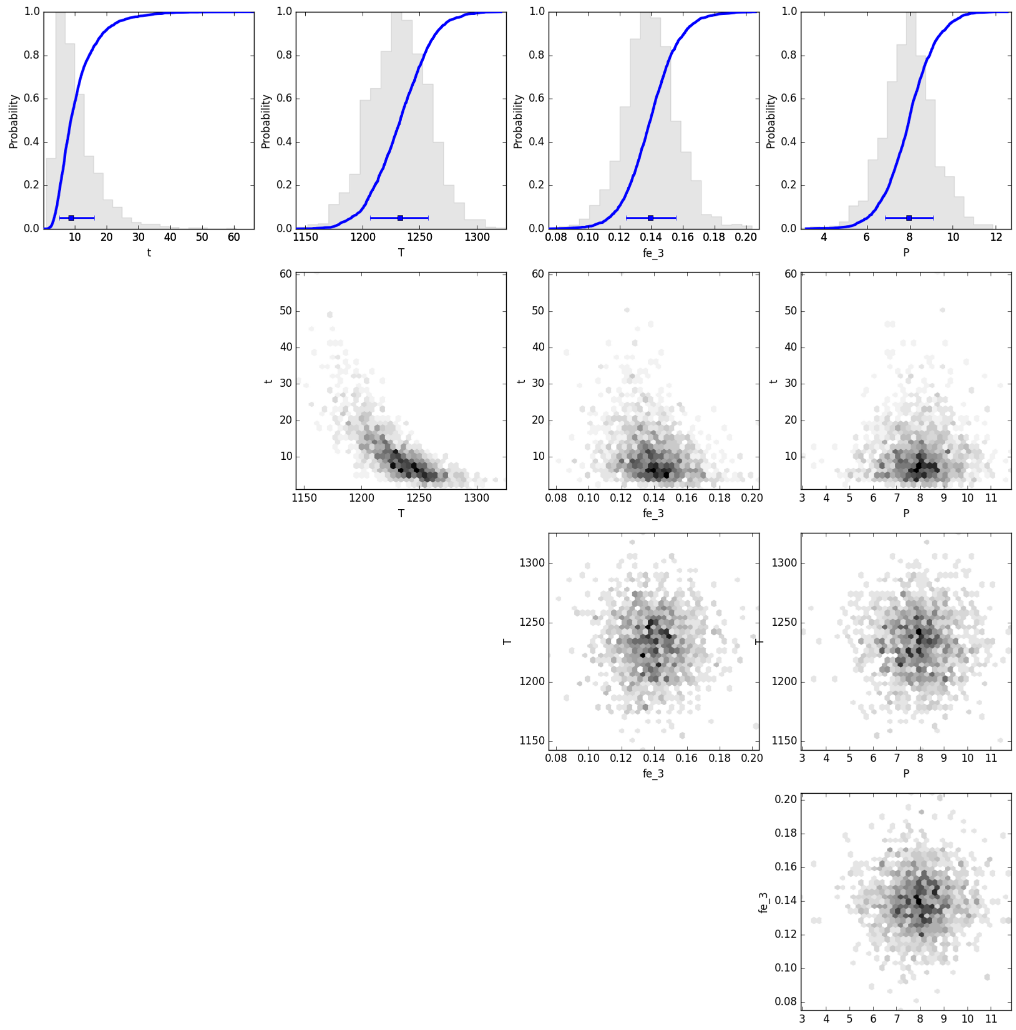

Supplementary Fig. 31: Bayesian inversion results for sample BORG_NOD1_N5_C1_P1. Marginal plot showing the posterior distributions of the Nested Sampling Bayesian Inversion for the main intensive parameters: t is time (days), T is temperature (°C), fe_3 is ferric iron content of the melt and P is pressure (kbar). The top row shows histograms (grey bars) and probablility density functions (blue curves) of the afformentioned intensive parameters. The blue bar shows the median result and 1σ standard deviation. The bottom three rows are density plots that show the trade offs between the different initensive parameters. These results are for models that used the Al-based (growth-controlled) initial conditions and $a_{\mathrm{SiO_2}}$ independent olivine diffusion equations.

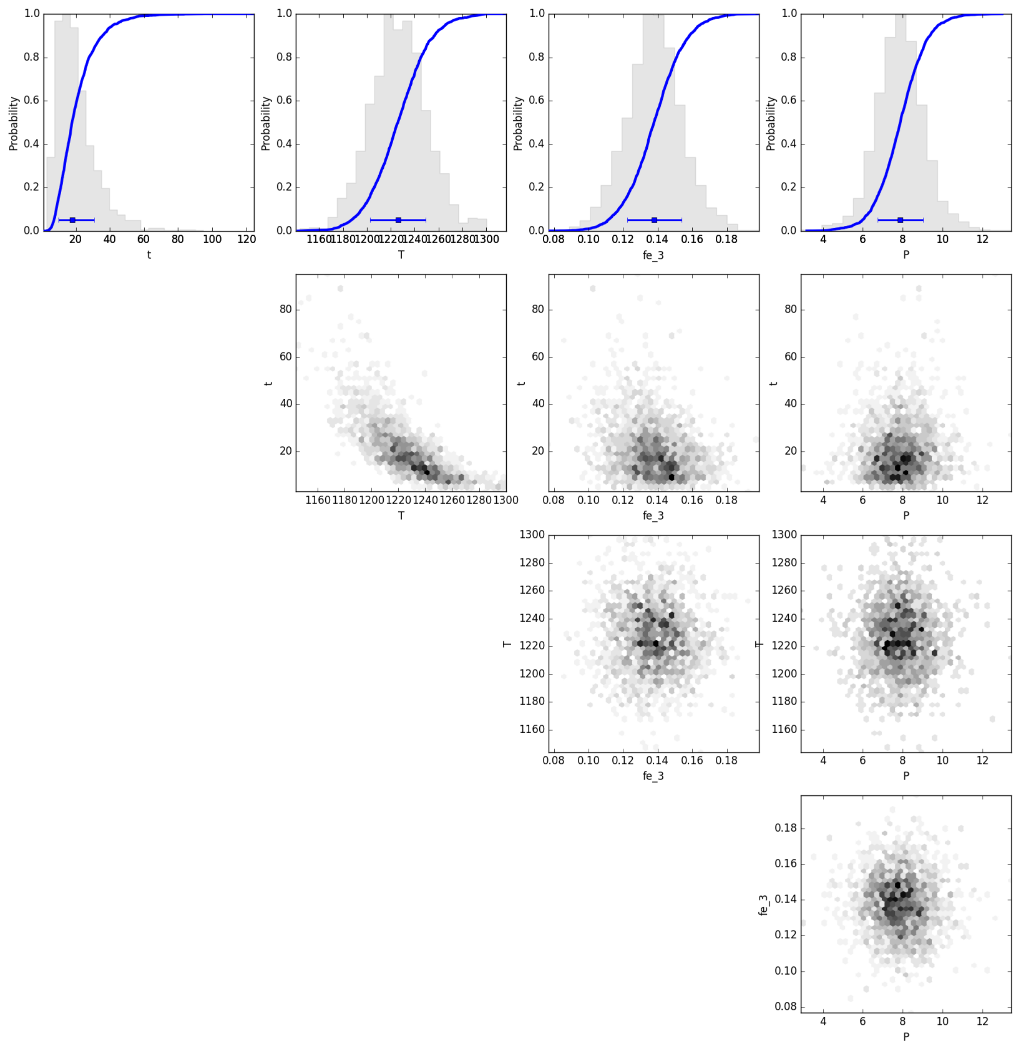

Supplementary Fig. 32: Bayesian inversion results for sample BORG_NOD1_N5_C2_P1. Marginal plot showing the posterior distributions of the Nested Sampling Bayesian Inversion for the main intensive parameters: t is time (days), T is temperature (°C), fe_3 is ferric iron content of the melt and P is pressure (kbar). The top row shows histograms (grey bars) and probablility density functions (blue curves) of the afformentioned intensive parameters. The blue bar shows the median result and 1σ standard deviation. The bottom three rows are density plots that show the trade offs between the different initensive parameters. These results are for models that used the Al-based (growth-controlled) initial conditions and $a_{\mathrm{SiO_2}}$ independent olivine diffusion equations.

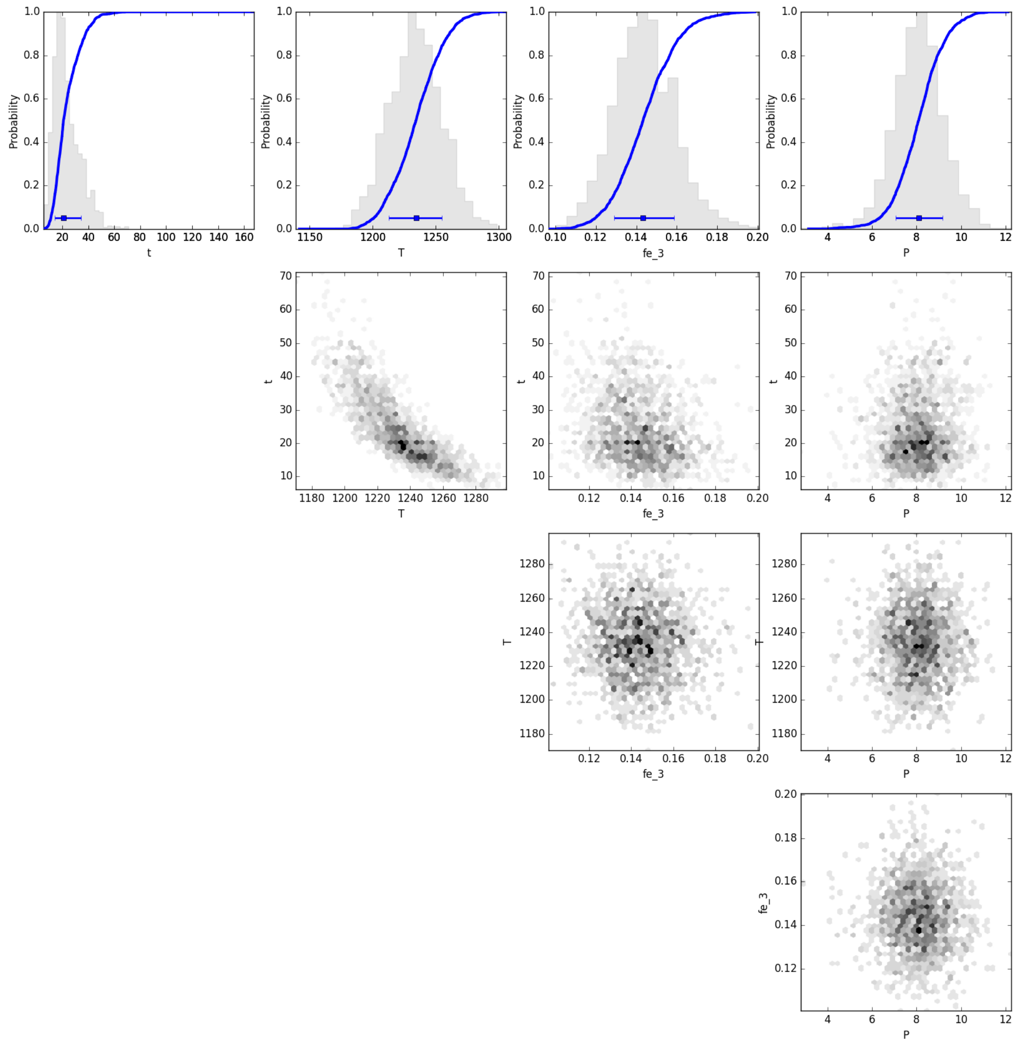

Supplementary Fig. 33: Bayesian inversion results for sample BORG_NOD1_N6_C2_P1. Marginal plot showing the posterior distributions of the Nested Sampling Bayesian Inversion for the main intensive parameters: t is time (days), T is temperature (°C), fe_3 is ferric iron content of the melt and P is pressure (kbar). The top row shows histograms (grey bars) and probablility density functions (blue curves) of the afformentioned intensive parameters. The blue bar shows the median result and 1σ standard deviation. The bottom three rows are density plots that show the trade offs between the different initensive parameters. These results are for models that used the Al-based (growth-controlled) initial conditions and $a_{\mathrm{SiO_2}}$ independent olivine diffusion equations.

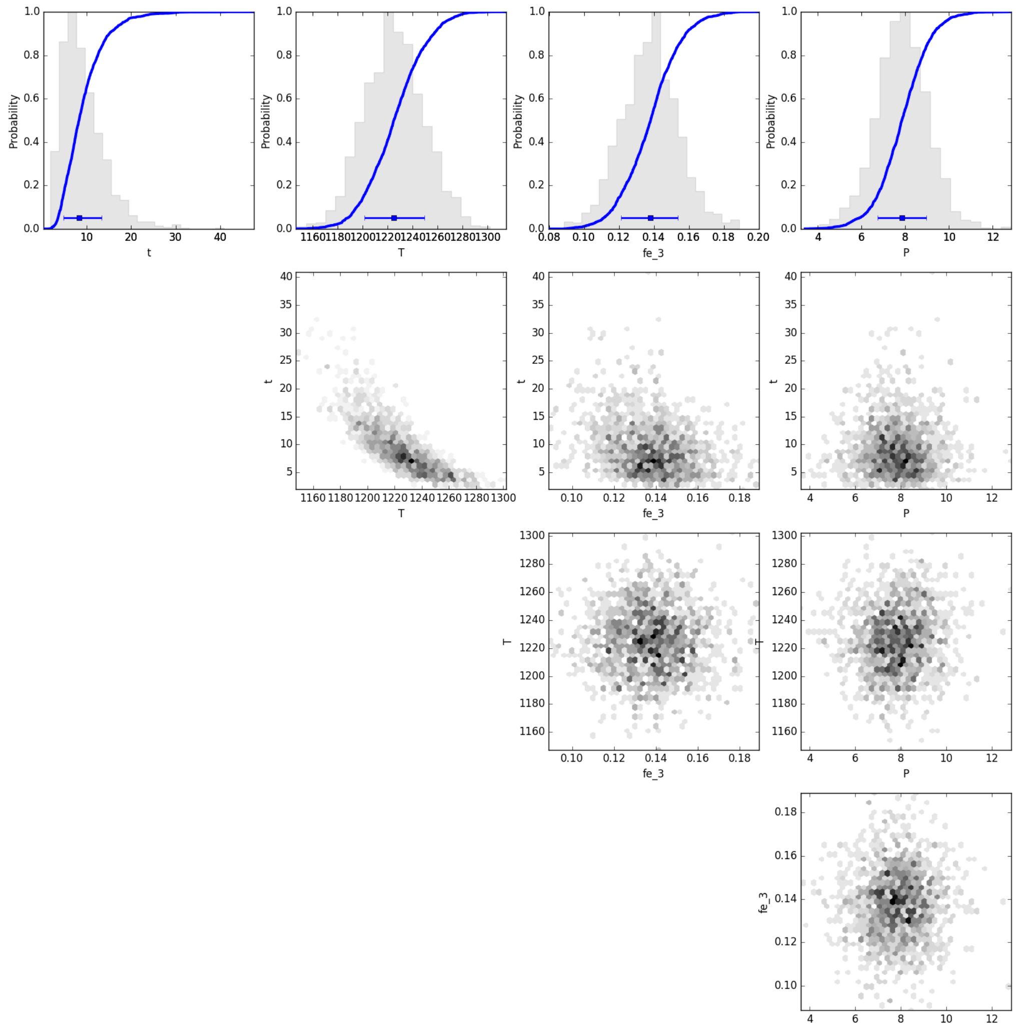

Supplementary Fig. 34: Bayesian inversion results for sample BORG_NOD2_N1_C3_P2. Marginal plot showing the posterior distributions of the Nested Sampling Bayesian Inversion for the main intensive parameters: t is time (days), T is temperature (°C), fe_3 is ferric iron content of the melt and P is pressure (kbar). The top row shows histograms (grey bars) and probablility density functions (blue curves) of the afformentioned intensive parameters. The blue bar shows the median result and 1σ standard deviation. The bottom three rows are density plots that show the trade offs between the different initensive parameters. These results are for models that used the Al-based (growth-controlled) initial conditions and $a_{\mathrm{SiO_2}}$ independent olivine diffusion equations.

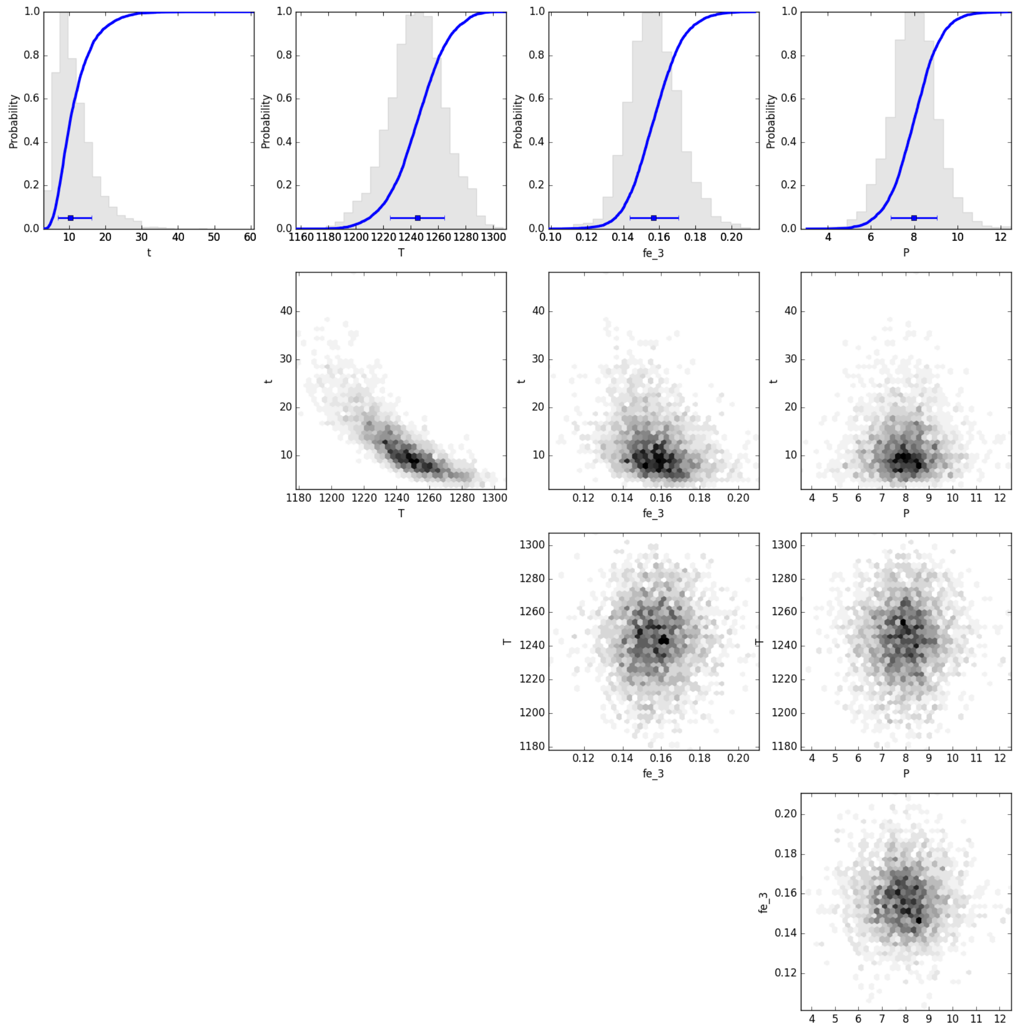

Supplementary Fig. 35: Bayesian inversion results for sample BORG_NOD2_N2_C4_P2. Marginal plot showing the posterior distributions of the Nested Sampling Bayesian Inversion for the main intensive parameters: t is time (days), T is temperature (°C), fe_3 is ferric iron content of the melt and P is pressure (kbar). The top row shows histograms (grey bars) and probablility density functions (blue curves) of the afformentioned intensive parameters. The blue bar shows the median result and 1σ standard deviation. The bottom three rows are density plots that show the trade offs between the different initensive parameters. These results are for models that used the Al-based (growth-controlled) initial conditions and $a_{\mathrm{SiO_2}}$ independent olivine diffusion equations.

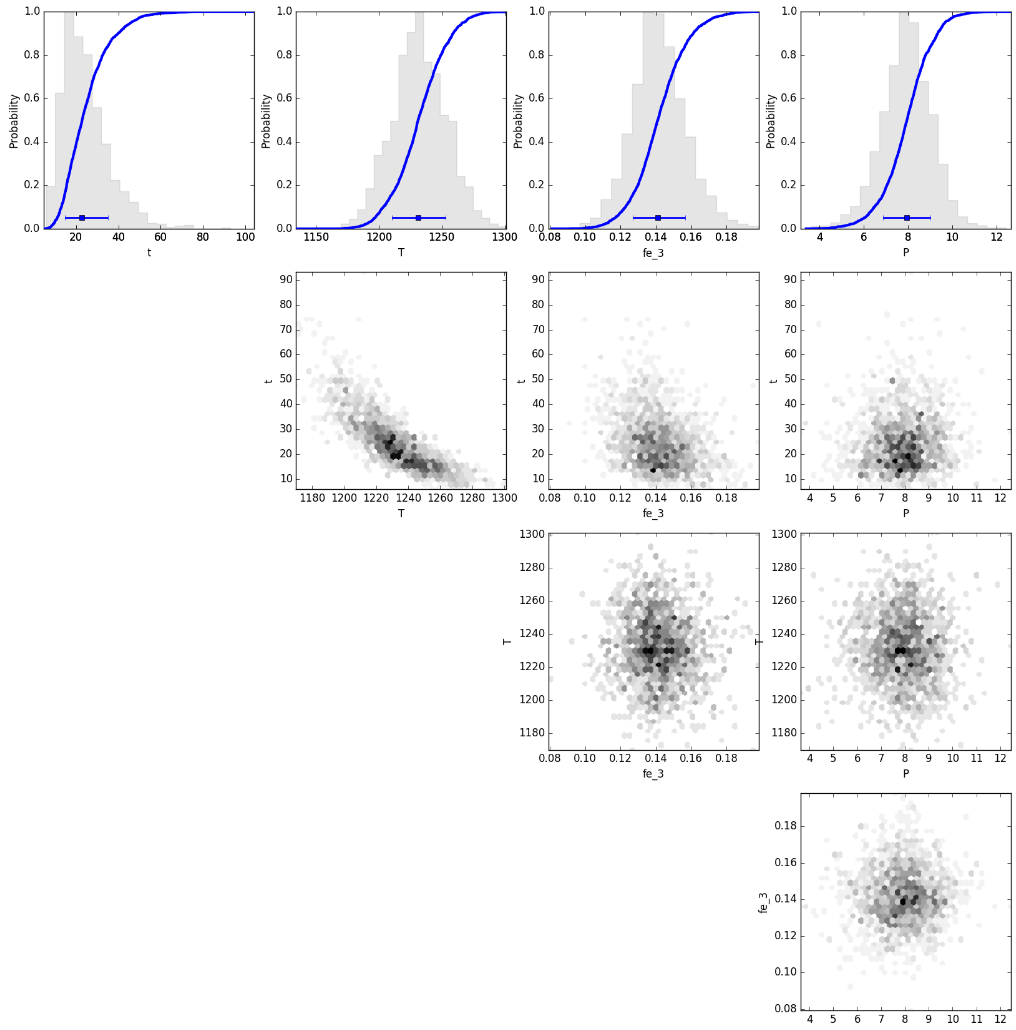

Supplementary Fig. 36: Bayesian inversion results for sample BORG_NOD2_N3_C2_P1. Marginal plot showing the posterior distributions of the Nested Sampling Bayesian Inversion for the main intensive parameters: t is time (days), T is temperature (°C), fe_3 is ferric iron content of the melt and P is pressure (kbar). The top row shows histograms (grey bars) and probablility density functions (blue curves) of the afformentioned intensive parameters. The blue bar shows the median result and 1σ standard deviation. The bottom three rows are density plots that show the trade offs between the different initensive parameters. These results are for models that used the Al-based (growth-controlled) initial conditions and a_{SiO_2} independent olivine diffusion equations.

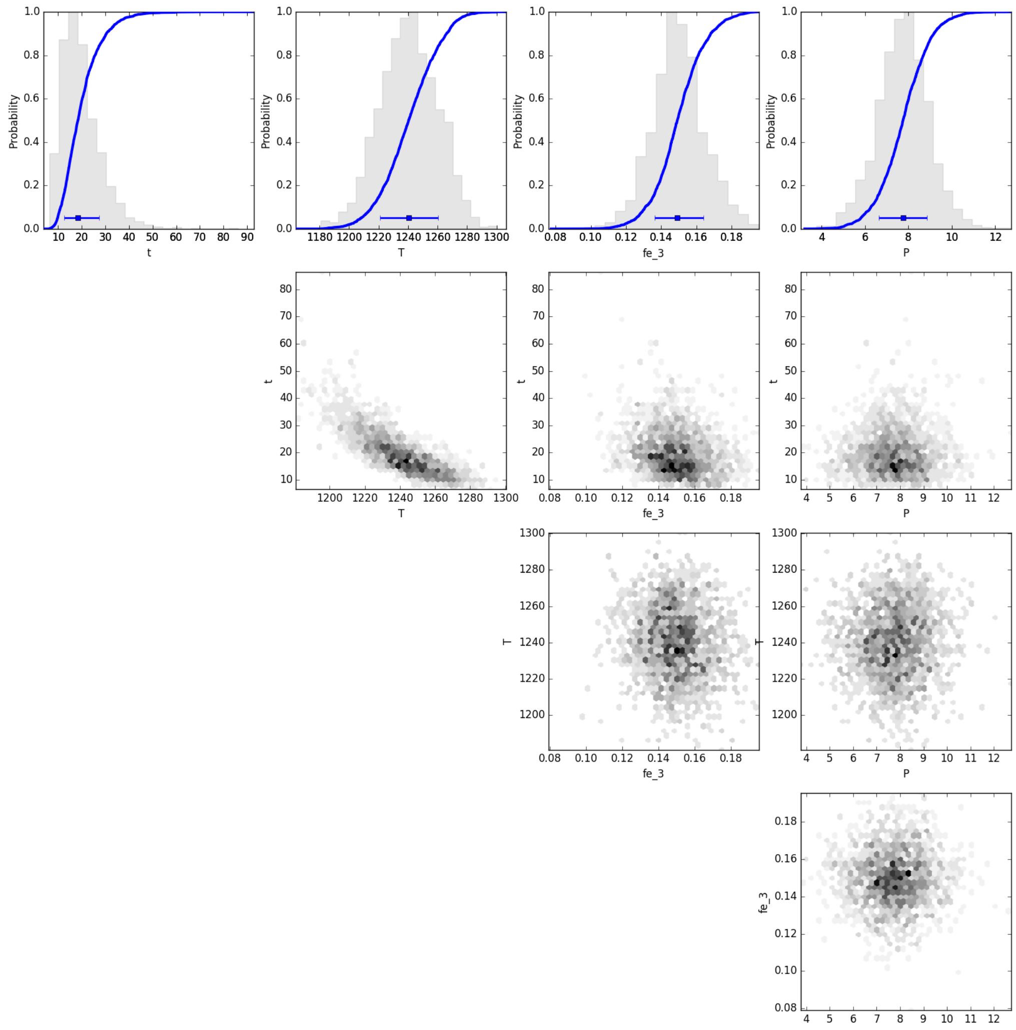

Supplementary Fig. 37: Bayesian inversion results for sample BORG_NOD2_N3_C6_P2. Marginal plot showing the posterior distributions of the Nested Sampling Bayesian Inversion for the main intensive parameters: t is time (days), T is temperature (°C), fe_3 is ferric iron content of the melt and P is pressure (kbar). The top row shows histograms (grey bars) and probablility density functions (blue curves) of the afformentioned intensive parameters. The blue bar shows the median result and 1σ standard deviation. The bottom three rows are density plots that show the trade offs between the different initensive parameters. These results are for models that used the Al-based (growth-controlled) initial conditions and $a_{\mathrm{SiO_2}}$ independent olivine diffusion equations.

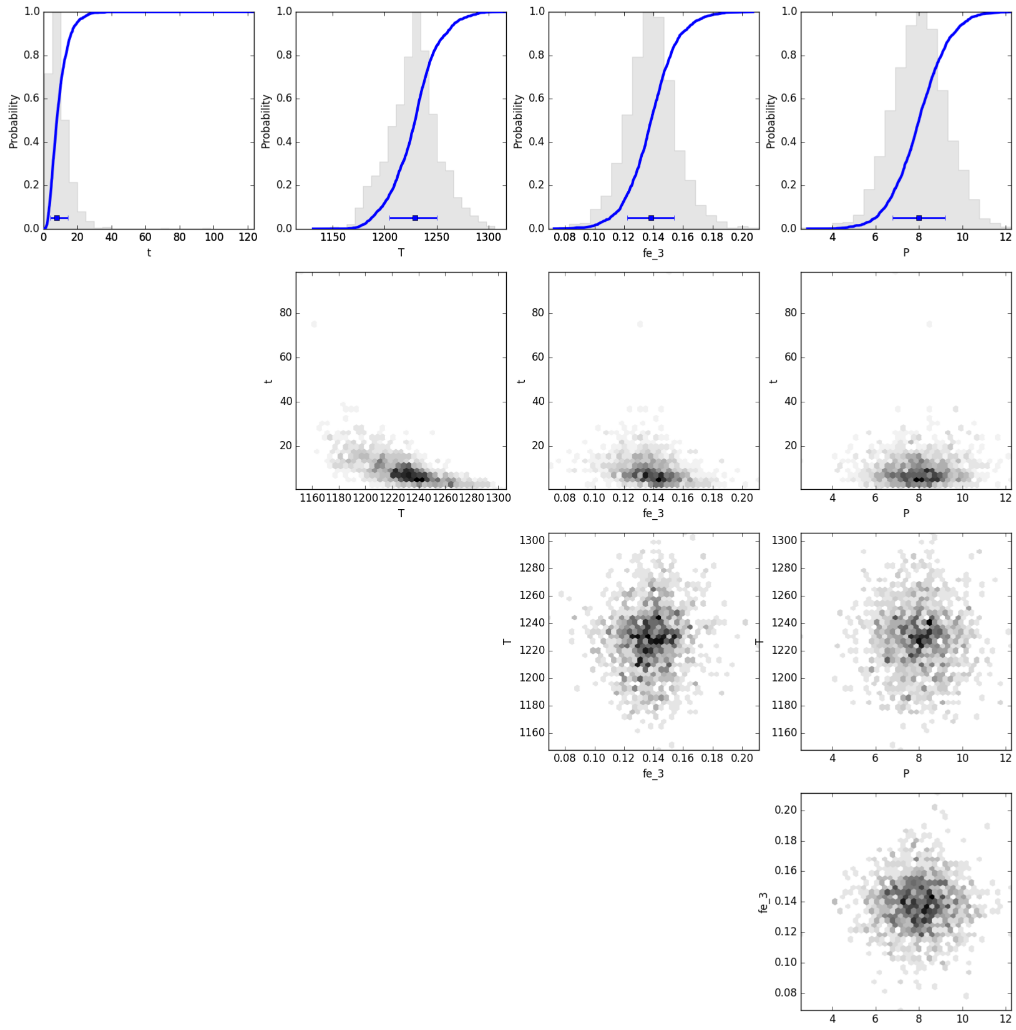

Supplementary Fig. 38: Bayesian inversion results for sample BORG_NOD3_N1_C1_P2. Marginal plot showing the posterior distributions of the Nested Sampling Bayesian Inversion for the main intensive parameters: t is time (days), T is temperature (°C), fe_3 is ferric iron content of the melt and P is pressure (kbar). The top row shows histograms (grey bars) and probablility density functions (blue curves) of the afformentioned intensive parameters. The blue bar shows the median result and 1σ standard deviation. The bottom three rows are density plots that show the trade offs between the different initensive parameters. These results are for models that used the Al-based (growth-controlled) initial conditions and $a_{\mathrm{SiO_2}}$ independent olivine diffusion equations.

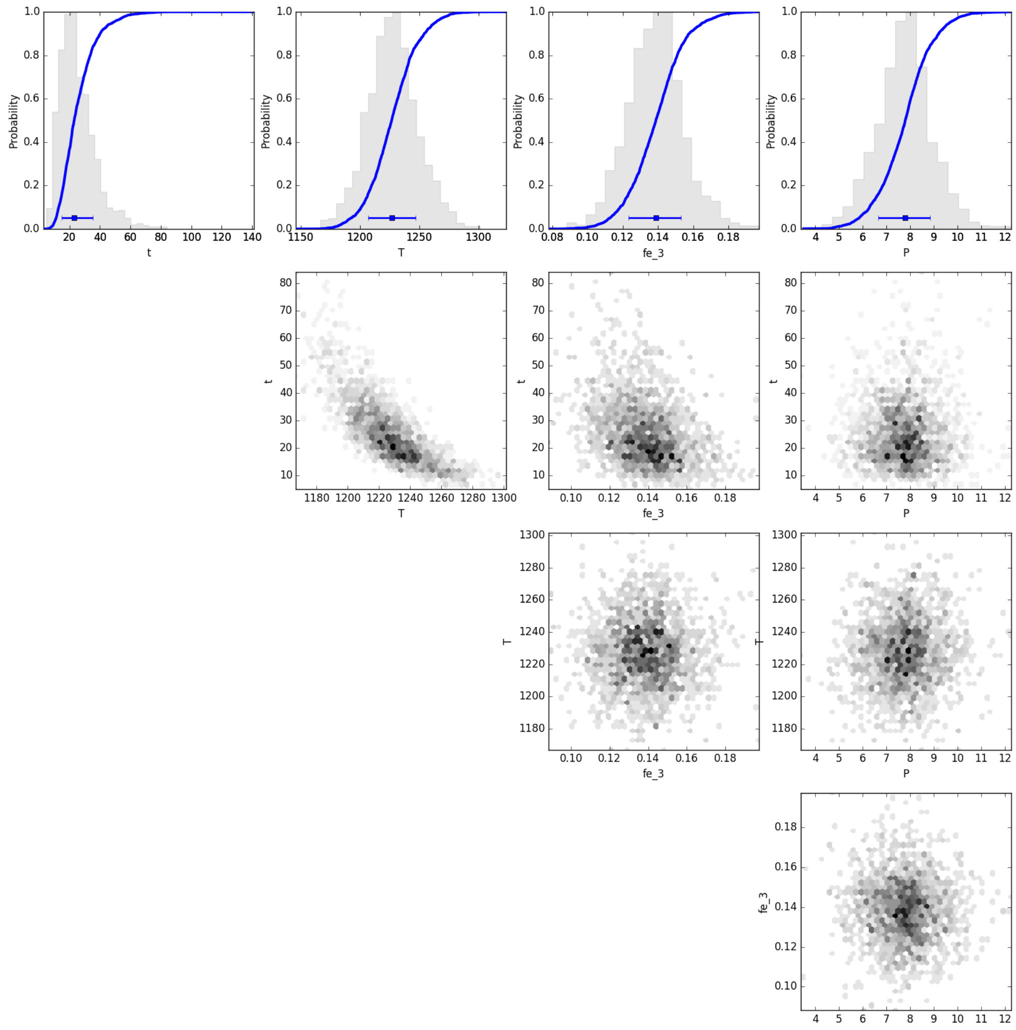

Supplementary Fig. 39: Bayesian inversion results for sample BORG_NOD3_N2_C1_P2. Marginal plot showing the posterior distributions of the Nested Sampling Bayesian Inversion for the main intensive parameters: t is time (days), T is temperature (°C), fe_3 is ferric iron content of the melt and P is pressure (kbar). The top row shows histograms (grey bars) and probablility density functions (blue curves) of the afformentioned intensive parameters. The blue bar shows the median result and 1σ standard deviation. The bottom three rows are density plots that show the trade offs between the different initensive parameters. These results are for models that used the Al-based (growth-controlled) initial conditions and $a_{\mathrm{SiO_2}}$ independent olivine diffusion equations.

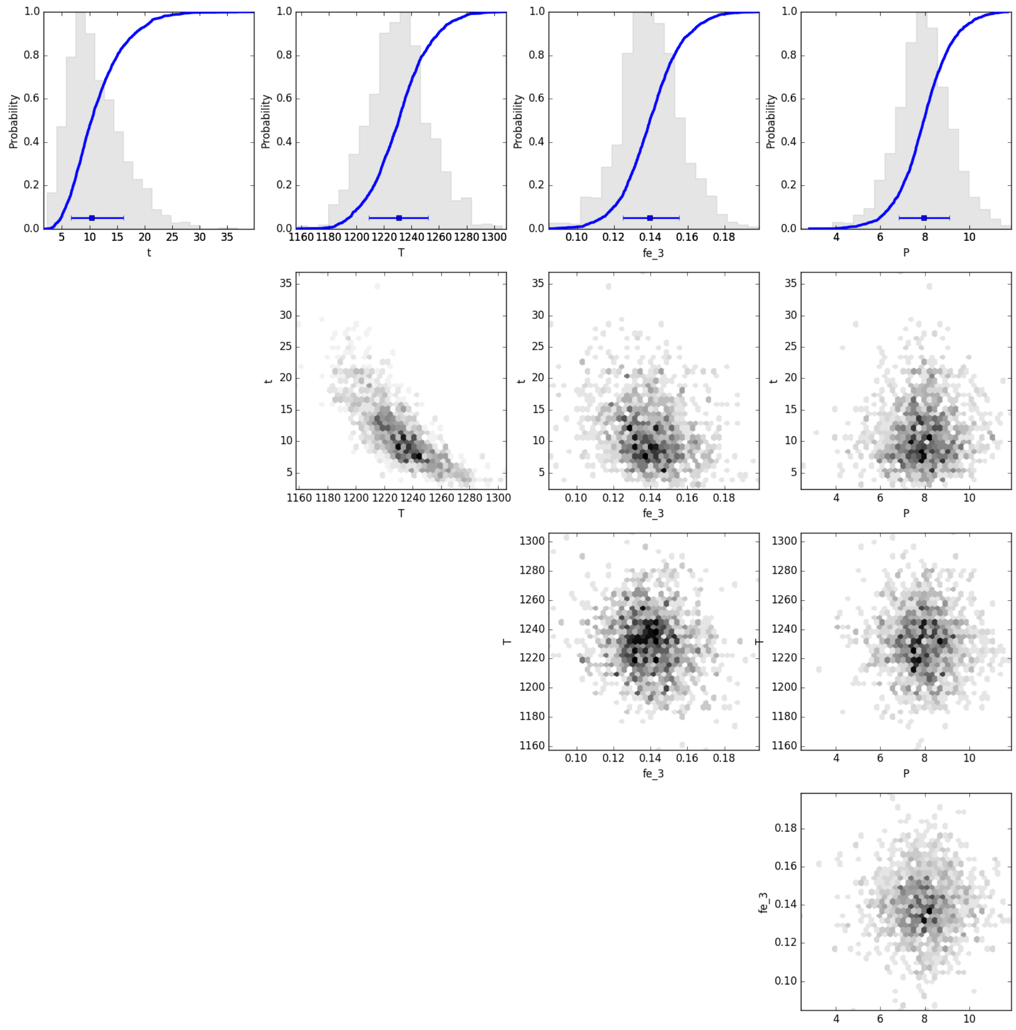

Supplementary Fig. 40: Bayesian inversion results for sample BORG_NOD3_N2_C2_P2. Marginal plot showing the posterior distributions of the Nested Sampling Bayesian Inversion for the main intensive parameters: t is time (days), T is temperature (°C), fe_3 is ferric iron content of the melt and P is pressure (kbar). The top row shows histograms (grey bars) and probablility density functions (blue curves) of the afformentioned intensive parameters. The blue bar shows the median result and 1σ standard deviation. The bottom three rows are density plots that show the trade offs between the different initensive parameters. These results are for models that used the Al-based (growth-controlled) initial conditions and $a_{\mathrm{SiO_2}}$ independent olivine diffusion equations.

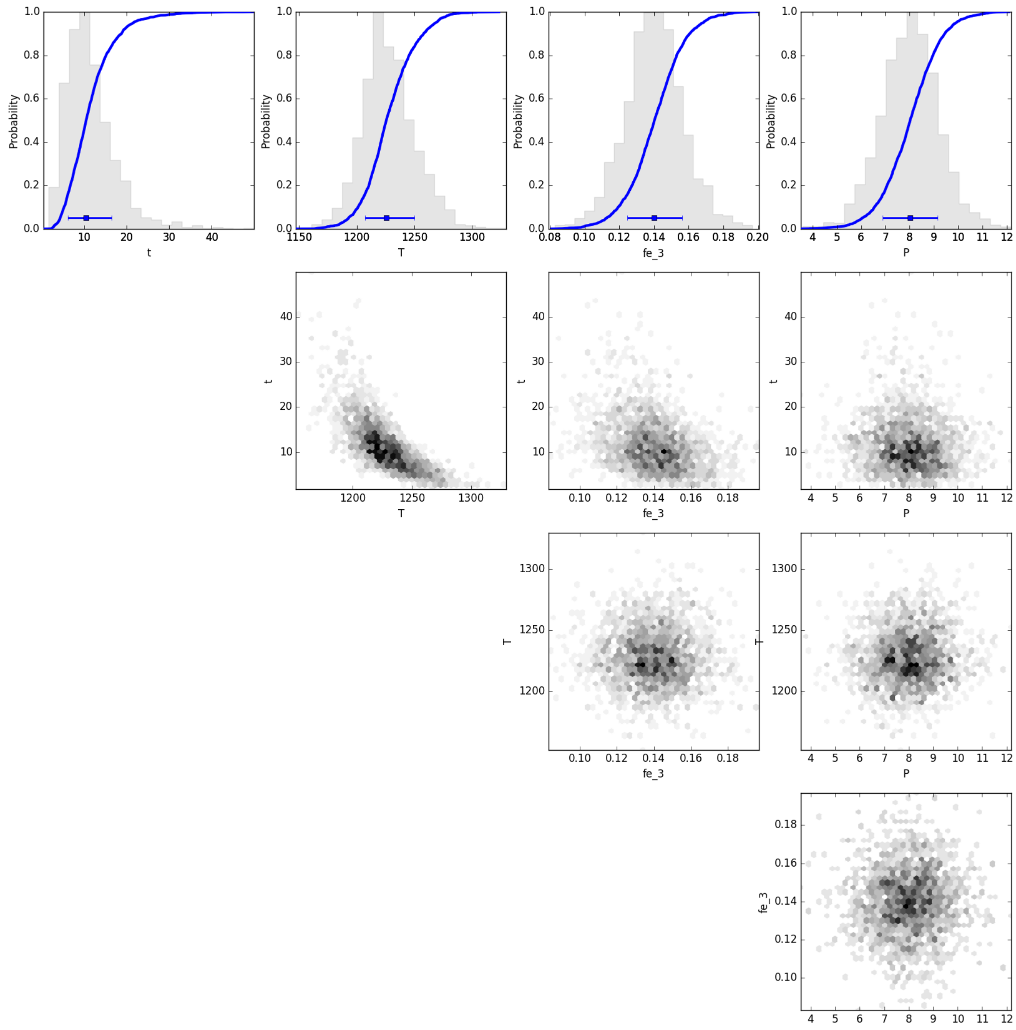

Supplementary Fig. 41: Bayesian inversion results for sample BORG_NOD3_N3_C1_P2. Marginal plot showing the posterior distributions of the Nested Sampling Bayesian Inversion for the main intensive parameters: t is time (days), T is temperature (°C), fe_3 is ferric iron content of the melt and P is pressure (kbar). The top row shows histograms (grey bars) and probablility density functions (blue curves) of the afformentioned intensive parameters. The blue bar shows the median result and 1σ standard deviation. The bottom three rows are density plots that show the trade offs between the different initensive parameters. These results are for models that used the Al-based (growth-controlled) initial conditions and $a_{\mathrm{SiO_2}}$ independent olivine diffusion equations.

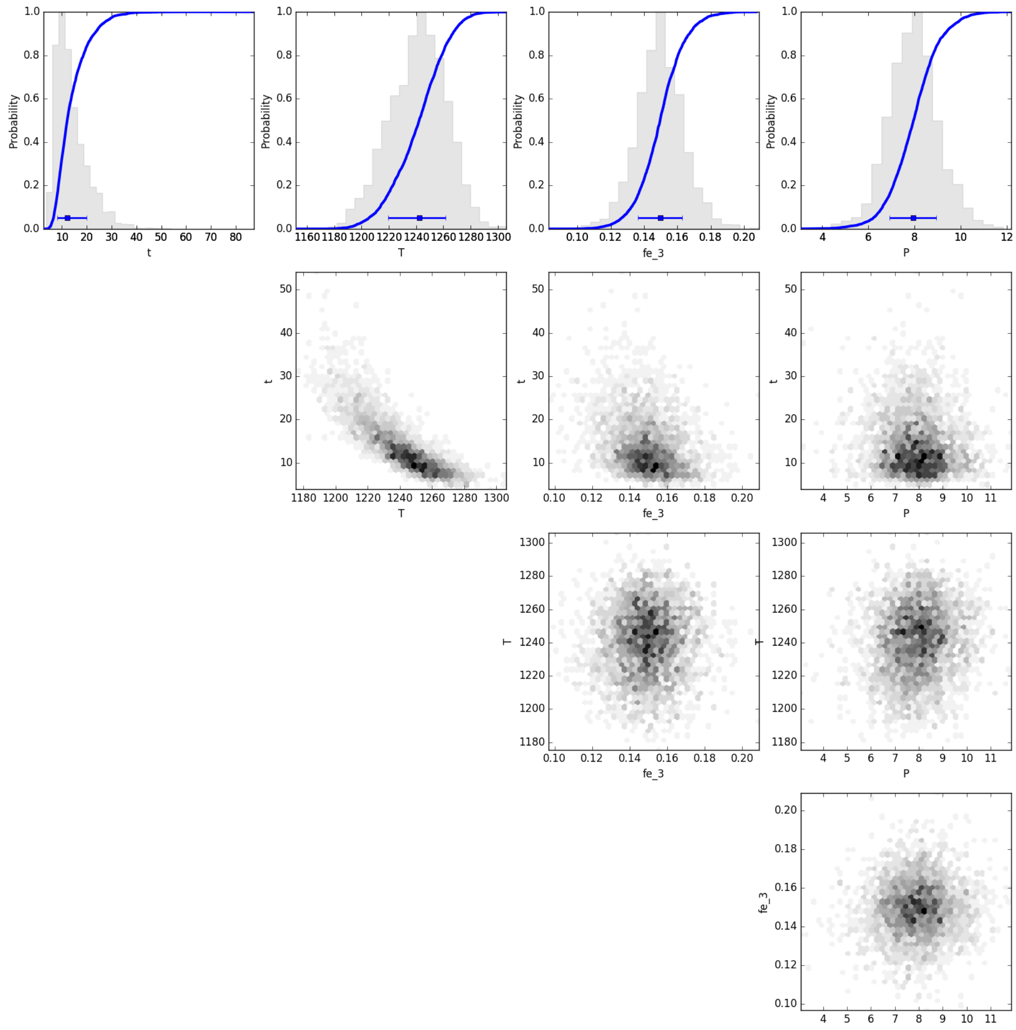

Supplementary Fig. 42: Bayesian inversion results for sample BORG_NOD3_N4_C1_P1. Marginal plot showing the posterior distributions of the Nested Sampling Bayesian Inversion for the main intensive parameters: t is time (days), T is temperature (°C), fe_3 is ferric iron content of the melt and P is pressure (kbar). The top row shows histograms (grey bars) and probablility density functions (blue curves) of the afformentioned intensive parameters. The blue bar shows the median result and 1σ standard deviation. The bottom three rows are density plots that show the trade offs between the different initensive parameters. These results are for models that used the Al-based (growth-controlled) initial conditions and $a_{\mathrm{SiO_2}}$ independent olivine diffusion equations.

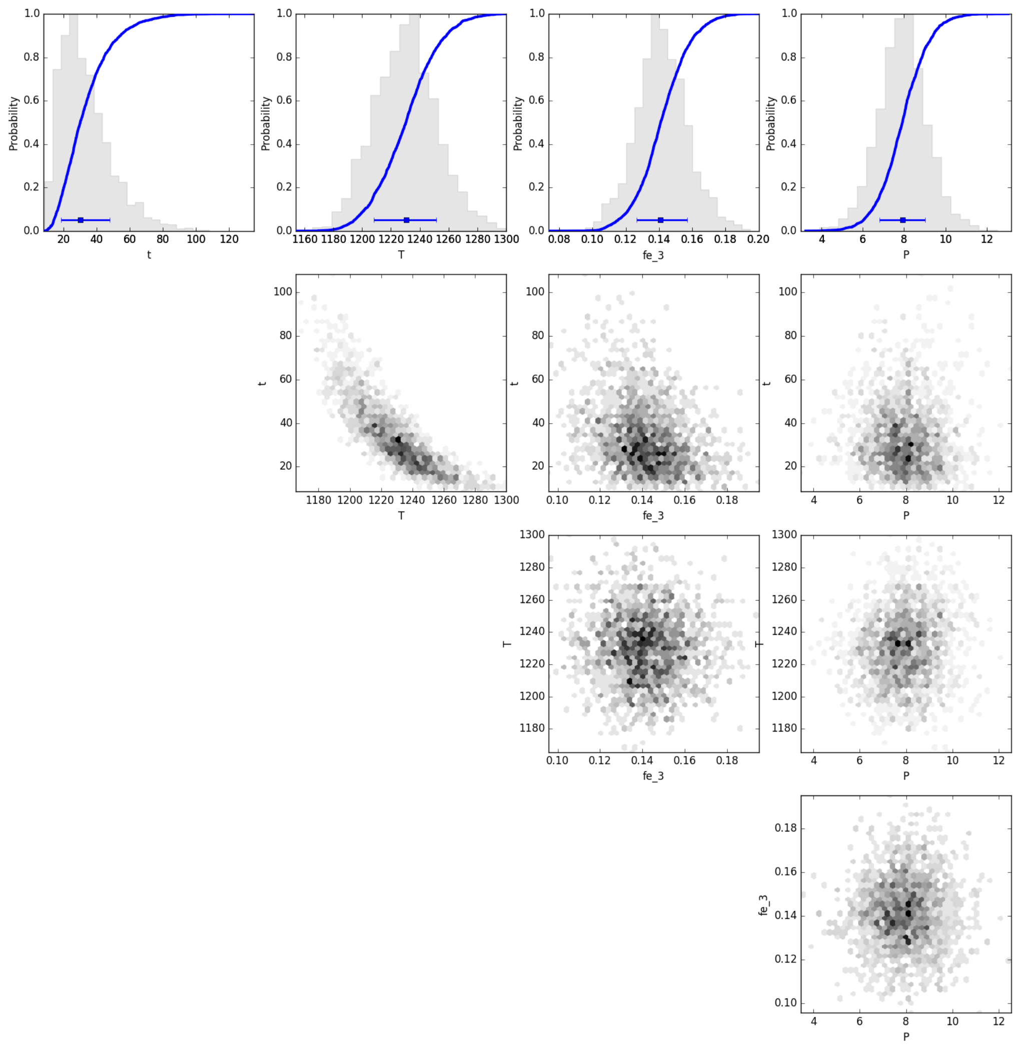

Supplementary Fig. 43: Bayesian inversion results for sample BORG_NOD3_N4_C3_P2. Marginal plot showing the posterior distributions of the Nested Sampling Bayesian Inversion for the main intensive parameters: t is time (days), T is temperature (°C), fe_3 is ferric iron content of the melt and P is pressure (kbar). The top row shows histograms (grey bars) and probablility density functions (blue curves) of the afformentioned intensive parameters. The blue bar shows the median result and 1σ standard deviation. The bottom three rows are density plots that show the trade offs between the different initensive parameters. These results are for models that used the Al-based (growth-controlled) initial conditions and $a_{\mathrm{SiO_2}}$ independent olivine diffusion equations.

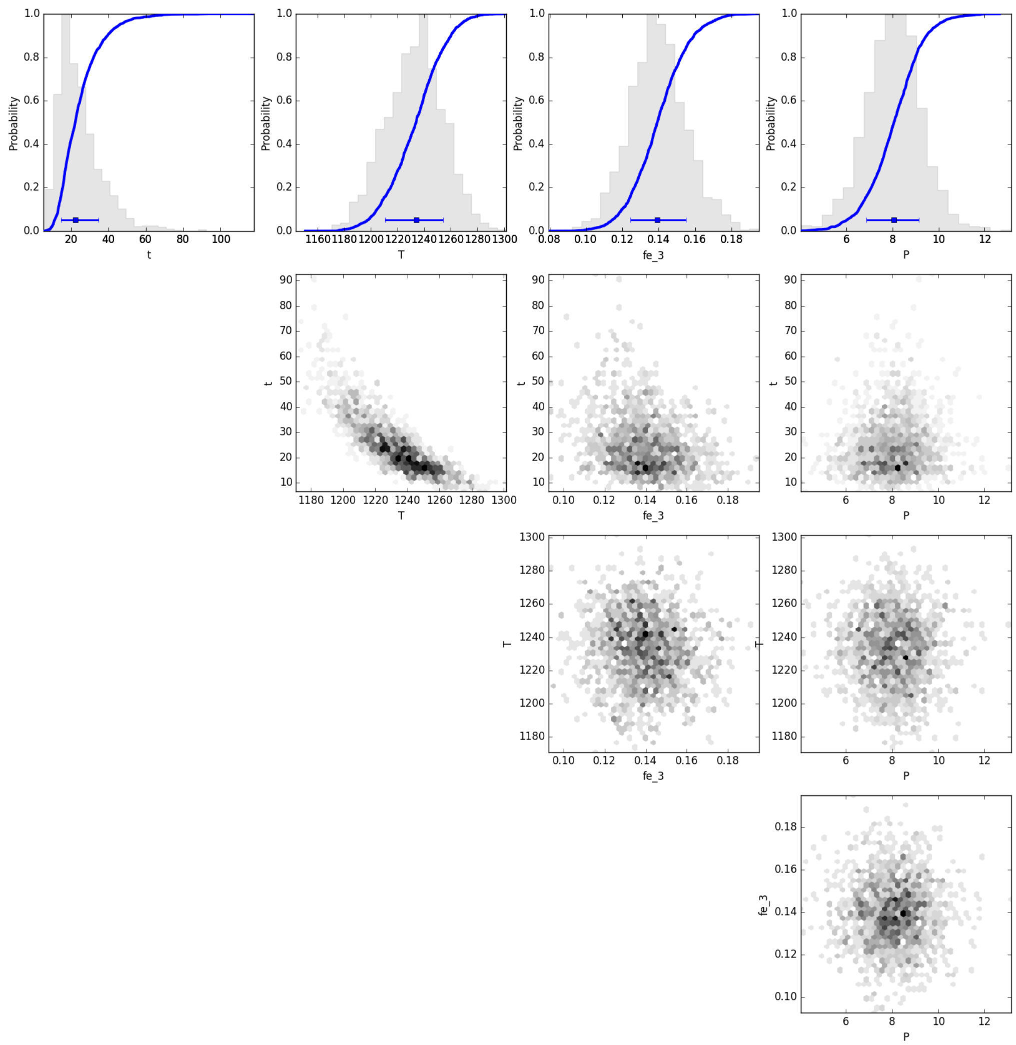

Supplementary Fig. 44: Bayesian inversion results for sample BORG_NOD3_N7_C1_P2. Marginal plot showing the posterior distributions of the Nested Sampling Bayesian Inversion for the main intensive parameters: t is time (days), T is temperature (°C), fe_3 is ferric iron content of the melt and P is pressure (kbar). The top row shows histograms (grey bars) and probablility density functions (blue curves) of the afformentioned intensive parameters. The blue bar shows the median result and 1σ standard deviation. The bottom three rows are density plots that show the trade offs between the different initensive parameters. These results are for models that used the Al-based (growth-controlled) initial conditions and $a_{\mathrm{SiO_2}}$ independent olivine diffusion equations.

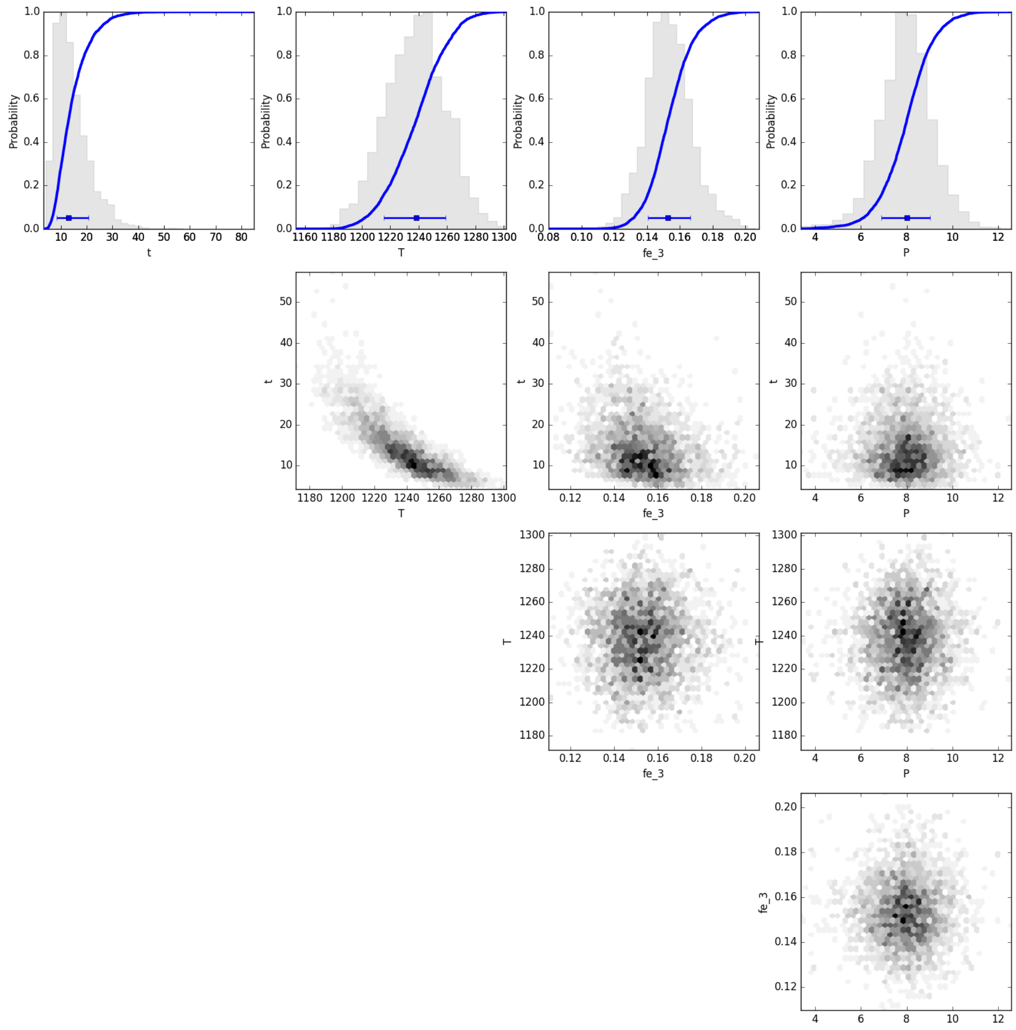

Supplementary Fig. 45: Bayesian inversion results for sample BORG_NOD5_N1_C1_P2. Marginal plot showing the posterior distributions of the Nested Sampling Bayesian Inversion for the main intensive parameters: t is time (days), T is temperature (°C), fe_3 is ferric iron content of the melt and P is pressure (kbar). The top row shows histograms (grey bars) and probablility density functions (blue curves) of the afformentioned intensive parameters. The blue bar shows the median result and 1σ standard deviation. The bottom three rows are density plots that show the trade offs between the different initensive parameters. These results are for models that used the Al-based (growth-controlled) initial conditions and $a_{\mathrm{SiO_2}}$ independent olivine diffusion equations.

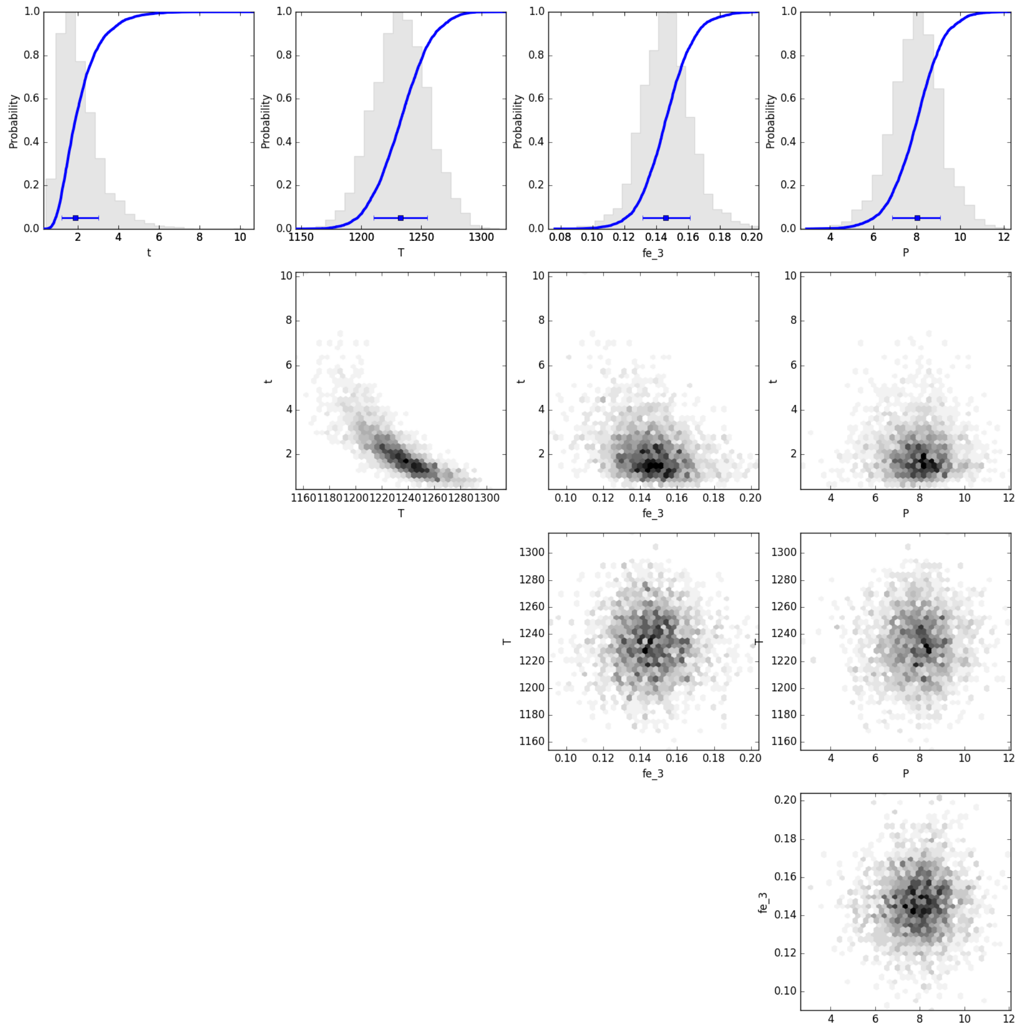

Supplementary Fig. 46: Bayesian inversion results for sample BORG_NOD5_N1_C2_P2. Marginal plot showing the posterior distributions of the Nested Sampling Bayesian Inversion for the main intensive parameters: t is time (days), T is temperature (°C), fe_3 is ferric iron content of the melt and P is pressure (kbar). The top row shows histograms (grey bars) and probablility density functions (blue curves) of the afformentioned intensive parameters. The blue bar shows the median result and 1σ standard deviation. The bottom three rows are density plots that show the trade offs between the different initensive parameters. These results are for models that used the Al-based (growth-controlled) initial conditions and $a_{\mathrm{SiO_2}}$ independent olivine diffusion equations.

Supplementary Tables

Supplementary Table 1: Olivine diffusion equation regression parameters derived and used as part of this study. The regressions were made from a compilation of olivine diffusion experimental data[24,30−34]. FeMg (Global) uses all of the FeMg diffusion data (both TaMED and PED olivine diffusion mechanisms). FeMg (TaMED) is the TaMED olivine diffusion mechanism. Ni ($a_{\mathrm{SiO_2}}$) and Mn ($a_{\mathrm{SiO_2}}$) are both regressions through experimental data that have been buffered for $a_{\mathrm{SiO_2}}$ [35,36].

Element	$\mathbf{a_i}$	$\mathbf{b_i}$	$\mathbf{c_i}$	$\mathbf{q_i}$	$\mathbf{j_i}$	$\mathbf{h_i}$	$\mathbf{k_i}$
FeMg (Global)	-7.86	0.187	-7.21	-26600	-4.15E-10	-1.54E-07	-
FeMg (TaMED)	-6.76	0.224	-7.18	-26700	-5.21E-10	-1.03E-07	-
Ni	-11.1	0.277	-2.19	-25100	-1.25E-09	9.97E-07	-
Mn	-7.55	0.196	-7.15	-26700	-9.5E-10	7.20E-07	-
Ni ($a_{\mathrm{SiO_2}}$)	-14.4	-0.107	-	-32980	-	-	0.714
Mn ($a_{\mathrm{SiO_2}}$)	-7.46	-0.097	-	-44310	-	-	0.761

Supplementary Table 2: Covariance matrices for olivine diffusion equations derived in this study. Parameters are the same as those presented in Supplementary Table 1. The regressions were made from a compilation of olivine diffusion experimental data[24,30−34].

	a_i	b_i	c_i	q_i	j_i	h_i
			FeMg (Global)			
a_i	4.97E-01	3.63E-03	-1.32E-01	-3.78E+02	-2.77E-11	2.69E-08
b_i	3.63E-03	4.31E-04	1.08E-03	1.02E+01	-6.41E-13	-1.99E-10
c_i	-1.32E-01	1.08E-03	1.49E-01	5.10E+01	-1.46E-13	-4.71E-09
q_i	-3.78E+02	1.02E+01	5.10E+01	8.40E+05	1.33E-08	-3.94E-05
j_i	-2.77E-11	-6.41E-13	-1.46E-13	1.33E-08	2.33E-19	-3.91E-16
h_i	2.69E-08	-1.99E-10	-4.71E-09	-3.94E-05	-3.91E-16	6.61E-13
			FeMg (TaMED)			
a_i	7.20E-01	1.36E-02	-1.37E-01	-3.17E+02	-5.11E-11	3.57E-08
b_i	1.36E-02	8.25E-04	2.25E-04	1.18E+01	-1.61E-12	2.07E-10
c_i	-1.37E-01	2.25E-04	1.34E-01	4.45E+01	1.76E-12	-5.05E-09
q_i	-3.17E+02	1.18E+01	4.45E+01	8.20E+05	8.12E-09	-3.61E-05
j_i	-5.11E-11	-1.61E-12	1.76E-12	8.12E-09	2.08E-19	-3.46E-16
h_i	3.57E-08	2.07E-10	-5.05E-09	-3.61E-05	-3.46E-16	5.83E-13
			Ni			
a_i	3.33E+00	1.09E-02	-1.77E+00	-2.19E+03	-1.40E-10	1.90E-07
b_i	1.09E-02	2.17E-03	-1.53E-02	8.50E+01	-1.98E-12	-1.98E-09
c_i	-1.77E+00	-1.53E-02	1.88E+00	-3.40E+02	2.68E-11	-2.61E-08
q_i	-2.19E+03	8.50E+01	-3.40E+02	6.79E+06	9.50E-08	-3.21E-04
j_i	-1.40E-10	-1.98E-12	2.68E-11	9.50E-08	2.23E-19	-3.69E-16
h_i	1.90E-07	-1.98E-09	-2.61E-08	-3.21E-04	-3.69E-16	6.25E-13
			Mn			
a_i	3.24E+00	3.94E-03	-6.79E-01	-3.68E+03	-1.95E-10	2.69E-07
b_i	3.94E-03	3.48E-03	2.78E-03	1.19E+02	-4.03E-12	-2.04E-09
c_i	-6.79E-01	2.78E-03	3.23E-01	7.26E+02	2.82E-11	-5.37E-08
q_i	-3.68E+03	1.19E+02	7.26E+02	8.79E+06	9.61E-08	-3.99E-04
j_i	-1.95E-10	-4.03E-12	2.82E-11	9.61E-08	2.83E-19	-4.65E-16
h_i	2.69E-07	-2.04E-09	-5.37E-08	-3.99E-04	-4.65E-16	7.87E-13

Supplementary Table 3: Covariance matrices for a_{SiO_2}-dependent olivine diffusion equations derived in this study. Parameters are the same as those presented in Supplementary Table 1. Regressions were made through experimental data that were buffered for a_{SiO_2} [35,36].

	a_i	b_i	k_i	q_i
		Ni		
a_i	2.15E+01	4.52E-02	2.02E-01	-3.42E+04
b_i	4.52E-02	1.04E-03	1.09E-03	-5.81E+01
k_i	2.02E-01	1.09E-03	2.26E-02	-2.23E+02
q_i	-3.42E+04	-5.81E+01	-2.23E+02	5.52E+07
		Mn		
a_i	6.09E+00	4.68E-03	5.01E-02	-9.81E+03
b_i	4.68E-03	1.33E-04	6.50E-05	-4.73E+00
k_i	5.01E-02	6.50E-05	7.76E-03	-4.65E+01
q_i	-9.81E+03	-4.73E+00	-4.65E+01	1.61E+07

Supplementary Table 4: Angles between the EPMA profile and the main crystallographic axes in olivine as measured by EBSD. These angles are incorporated into the anisotropy calculation used to determine the apparent diffusivity parallel to the measured profile. angle100P, angle010P and angle001P are the angles between the profile and [100], [010] and [001] respectively.

Profile	**angle100P** (°)	**angle010P** (°)	**angle001P** (°)
BORG14_OL_C2_P1	102.64	16.69	100.72
BORG14_OL_C25_P1	106.63	162.63	94.88
BORG_NOD1_N2_C1_P1	71.49	19.12	94.64
BORG_NOD1_N3_C1_P2	87.00	50.78	39.38
BORG_NOD1_N5_C1_P1	153.11	107.52	109.73
BORG_NOD1_N5_C2_P1	130.73	137.88	81.07
BORG_NOD1_N6_C2_P1	123.45	135.33	64.12
BORG_NOD2_N1_C3_P2	37.31	84.43	53.25
BORG_NOD2_N2_C4_P2	67.75	34.01	114.31
BORG_NOD2_N3_C2_P1	71.51	96.28	19.60
BORG_NOD2_N3_C6_P2	77.45	116.32	150.41
BORG_NOD3_N1_C1_P2	80.27	12.64	82.00
BORG_NOD3_N2_C1_P2	50.97	137.54	104.09
BORG_NOD3_N2_C2_P2	42.28	64.28	59.06
BORG_NOD3_N3_C1_P2	54.76	39.57	105.67
BORG_NOD3_N4_C1_P1	42.06	130.48	80.47
BORG_NOD3_N4_C3_P2	139.46	119.51	115.10
BORG_NOD3_N7_C1_P2	99.18	140.98	52.48
BORG_NOD5_N1_C1_P2	27.55	116.93	84.64
BORG_NOD5_N1_C2_P2	70.38	118.75	144.08

Supplementary Table 5: Median timescales and 1σ errors obtained from the posterior distributions of the Nested Sampling Bayesian inversion conducted on each olivine profile. The results using Al-based initial conditions (Al-based IC), constant initial conditions (diffusion only, Constant IC), and a_{SiO_2} based equations using Al-based initial conditions (Al-based IC a_{SiO_2}) are presented here. The classification of each profile (growth-dominated vs. Al-decoupled) is also shown.

		Al-based IC (days)			**Constant IC (days)**			**Al-based IC a_{SiO_2} (days)**		
Profile	**Type**	**Median**	**+ 1σ**	**- 1σ**	**Median**	**+ 1σ**	**- 1σ**	**Median**	**+ 1σ**	**- 1σ**
BORG14_OL_C2_P1	Growth-dominated	12.27	7.82	4.70	46.82	20.12	14.41	13.84	9.05	5.59
BORG14_OL_C25_P1	Al-decoupled	23.89	13.90	8.62	34.31	18.53	11.63	32.65	18.65	12.83
BORG_NOD1_N2_C1_P1	Growth-dominated	5.29	4.85	3.17	14.92	9.65	5.82	4.59	4.11	2.86
BORG_NOD1_N3_C1_P2	Growth-dominated	1.48	1.41	0.77	5.57	3.40	2.09	1.50	1.60	0.81
BORG_NOD1_N5_C1_P1	Al-decoupled	8.76	7.24	3.74	20.51	10.40	7.67	7.90	5.26	3.44
BORG_NOD1_N5_C2_P1	Al-decoupled	17.82	12.86	7.80	25.48	15.27	9.53	15.50	11.47	6.53
BORG_NOD1_N6_C2_P1	Al-decoupled	20.96	13.49	6.60	24.43	12.02	8.40	20.15	12.98	8.18
BORG_NOD2_N1_C3_P2	Growth-dominated	8.34	5.12	3.49	46.43	24.35	17.15	6.04	3.66	2.20
BORG_NOD2_N2_C4_P2	Al-decoupled	10.37	5.92	3.33	23.29	11.29	7.92	21.54	11.42	7.89
BORG_NOD2_N3_C2_P1	Al-decoupled	22.85	12.27	8.19	47.29	24.68	18.29	16.81	10.00	5.80
BORG_NOD2_N3_C6_P2	Al-decoupled	18.40	8.84	5.94	45.57	23.88	15.83	20.17	10.72	7.53
BORG_NOD3_N1_C1_P2	Growth-dominated	7.80	6.46	3.65	36.35	24.54	13.73	6.38	4.94	3.26
BORG_NOD3_N2_C1_P2	Al-decoupled	23.06	12.43	8.20	61.14	31.75	20.72	20.56	11.15	7.37
BORG_NOD3_N2_C2_P2	Al-decoupled	10.37	5.74	3.74	14.93	8.38	5.28	8.40	4.86	3.15
BORG_NOD3_N3_C1_P2	Al-decoupled	10.48	5.95	4.30	18.72	10.45	7.37	8.74	6.30	3.32
BORG_NOD3_N4_C1_P1	Al-decoupled	12.19	7.85	3.98	19.03	9.34	6.66	15.67	8.69	5.57
BORG_NOD3_N4_C3_P2	Al-decoupled	30.04	17.88	11.46	45.56	23.41	15.67	27.44	16.04	10.52
BORG_NOD3_N7_C1_P2	Al-decoupled	22.33	12.48	7.71	44.61	22.85	16.14	17.04	8.90	5.40
BORG_NOD5_N1_C1_P2	Growth-dominated	12.95	7.71	4.51	16.86	8.52	5.21	15.04	9.05	5.44
BORG_NOD5_N1_C2_P2	Growth-dominated	1.87	1.14	0.68	4.25	2.46	1.44	2.22	1.34	0.88

References

1. Cashman, K. V., Sparks, R. S. J. & Blundy, J. D. Vertically extensive and unstable magmatic systems: a unified view of igneous processes. *Science* **355**, eaag3055 (2017).

2. Kelemen, P. B., Koga, K. & Shimizu, N. Geochemistry of gabbro sills in the crust-mantle transition zone of the Oman ophiolite: Implications for the origin of the oceanic lower crust. *Earth and Planetary Science Letters* **146**, 475–488 (1997).

3. Costa, F. & Dungan, M. Short time scales of magmatic assimilation from diffusion modeling of multiple elements in olivine.*Geology* **33**, 837–840 (2005).

4. Costa, F., Coogan, L. A. & Chakraborty, S. The time scales of magma mixing and mingling involving primitive melts and melt–mush interaction at mid-ocean ridges. *Contributions to Mineralogy and Petrology* **159**, 371–387 (2010).

5. Kahl, M., Chakraborty, S., Costa, F. & Pompilio, M. Dynamic plumbing system beneath volcanoes revealed by kinetic modeling, and the connection to monitoring data: An example from Mt. Etna. *Earth and Planetary Science Letters* **308**, 11–22 (2011).

6. Rae, A. S. *et al.* Time scales of magma transport and mixing at Kīlauea volcano, Hawai'i. *Geology* **44**, 463–466 (2016).

7. Hartley, M. E., Morgan, D. J., Maclennan, J., Edmonds, M. & Thordarson, T. Tracking timescales of short-term precursors to large basaltic fissure eruptions through Fe–Mg diffusion in olivine. *Earth and Planetary Science Letters* **439**, 58–70 (2016).

8. Pankhurst, M. J., Morgan, D. J., Thordarson, T. & Loughlin, S. C. Magmatic crystal records in time, space, and process, causatively linked with volcanic unrest.*Earth and Planetary Science Letters* **493**, 231–241 (2018).

9. Peslier, A. H., Woodland, A. B. & Wolff, J. A. Fast kimberlite ascent rates estimated from hydrogen diffusion profiles in xenolithic mantle olivines from southern Africa.*Geochimica et Cosmochimica Acta* **72**, 2711–2722 (2008).

10. Demouchy, S., Jacobsen, S. D., Gaillard, F. & Stern, C. R. Rapid magma ascent recorded by water diffusion profiles in mantle olivine. *Geology* **34**, 429–432 (2006).

11. Peslier, A. H., Bizimis, M. & Matney, M. Water disequilibrium in olivines from Hawaiian peridotites: Recent metasomatism, H diffusion and magma ascent rates. *Geochimica et Cosmochimica Acta* **154**, 98–117 (2015).

12. Ruprecht, P. & Plank, T. Feeding andesitic eruptions with a high-speed connection from the mantle.*Nature* **500**, 68 (2013).

13. Staples, R. K. *et al.* Faeroe-Iceland Ridge Experiment 1. Crustal structure of northeastern Iceland. *Journal of Geophysical Research: Solid Earth* **102**, 7849–7866 (1997).

14. Maclennan, J. *et al.* Melt mixing and crystallization under Theistareykir, northeast Iceland. *Geochemistry, Geophysics, Geosystems* **4**, 11 (2003).

15. Winpenny, B. & Maclennan, J. A partial record of mixing of mantle melts preserved in Icelandic phenocrysts. *Journal of Petrology* **52**, 1791–1812 (2011).

16. Neave, D. A. & Putirka, K. D. A new clinopyroxene-liquid barometer, and implications for magma storage pressures under Icelandic rift zones. *American Mineralogist* **102**, 777–794 (2017).

17. Maclennan, J., McKenzie, D., Hilton, F., Gronvöld, K. & Shimizu, N. Geochemical variability in a single flow from northern Iceland. *Journal of Geophysical Research: Solid Earth* **108**, B1 (2003).

18. Bender, J., Hodges, F. & Bence, A. Petrogenesis of basalts from the project FAMOUS area: experimental study from 0 to 15 kbars. *Earth and Planetary Science Letters* **41**, 277–302 (1978).

19. Weaver, J. S. & Langmuir, C. H. Calculation of phase equilibrium in mineral-melt systems.*Computers & Geosciences* **16**, 1–19 (1990).

20. Hauri, E. H. *et al.* CO_2 content beneath northern Iceland and the variability of mantle carbon. *Geology* **46**, 55–58 (2018).

21. Thomson, A. & Maclennan, J. The distribution of olivine compositions in Icelandic basalts and picrites.*Journal of Petrology* **54**, 745–768 (2012).

22. Dohmen, R., Faak, K. & Blundy, J. D. Chronometry and speedometry of magmatic processes using chemical diffusion in olivine, plagioclase and pyroxenes. *Reviews in Mineralogy and Geochemistry* **83**, 535–575 (2017).

23. Shea, T., Lynn, K. J. & Garcia, M. O. Cracking the olivine zoning code: Distinguishing between crystal growth and diffusion. *Geology* **43**, 935–938 (2015).

24. Spandler, C. & O'Neill, H. S. C. Diffusion and partition coefficients of minor and trace elements in San Carlos olivine at 1,300 °C with some geochemical implications. *Contributions to Mineralogy and Petrology* **159**, 791–818 (2010).

25. Zhukova, I., O'Neill, H. & Campbell, I. H. A subsidiary fast-diffusing substitution mechanism of Al in forsterite investigated using diffusion experiments under controlled thermodynamic conditions. *Contributions to Mineralogy and Petrology* **172**, 53 (2017).

26. Alnæs, M. *et al.* The FEniCS project version 1.5. *Archive of Numerical Software* **3**, 9–23 (2015).

27. Feroz, F., Hobson, M. & Bridges, M. MultiNest: an efficient and robust Bayesian inference tool for cosmology and particle physics. *Monthly Notices of the Royal Astronomical Society* **398**, 1601–1614 (2009).

28. Sugawara, T. Empirical relationships between temperature, pressure, and MgO content in olivine and pyroxene saturated liquid. *Journal of Geophysical Research: Solid Earth* **105**, 8457–8472 (2000).

29. Shorttle, O. *et al.* Fe-XANES analyses of Reykjanes Ridge basalts: Implications for oceanic crust's role in the solid Earth oxygen cycle. *Earth and Planetary Science Letters* **427**, 272–285 (2015).

30. Chakraborty, S. Rates and mechanisms of Fe–Mg interdiffusion in olivine at 980–1300 °C.*Journal of Geophysical Research: Solid Earth* **102**, 12317–12331 (1997).

31. Petry, C., Chakraborty, S. & Palme, H. Experimental determination of Ni diffusion coefficients in olivine and their dependence on temperature, composition, oxygen fugacity, and crystallographic orientation. *Geochimica et Cosmochimica Acta* **68**, 4179–4188 (2004).

32. Dohmen, R., Becker, H.-W. & Chakraborty, S. Fe–Mg diffusion in olivine I: experimental determination between 700 and 1,200 °C as a function of composition, crystal orientation and oxygen fugacity. *Physics and Chemistry of Minerals* **34**, 389–407 (2007).

33. Dohmen, R. & Chakraborty, S. Fe–Mg diffusion in olivine II: point defect chemistry, change of diffusion mechanisms and a model for calculation of diffusion coefficients in natural olivine. *Physics and Chemistry of Minerals* **34**, 409–430 (2007).

34. Holzapfel, C., Chakraborty, S., Rubie, D. & Frost, D. Effect of pressure on Fe–Mg, Ni and Mn diffusion in $(Fe_xMg_{1-x})_2SiO_4$ olivine. *Physics of the Earth and Planetary Interiors* **162**, 186–198 (2007).

35. Zhukova, I., O'Neill, H. S. C., Campbell, I. H. & Kilburn, M. R. The effect of silica activity on the diffusion of Ni and Co in olivine. *Contributions to Mineralogy and Petrology* **168**, 1029 (2014).

36. Jollands, M., Hermann, J., O'Neill, H. S. C., Spandler, C. & Padrón-Navarta, J. Diffusion of Ti and some divalent cations in olivine as a function of temperature, oxygen fugacity, chemical potentials and crystal orientation. *Journal of petrology* **57**, 1983–2010 (2016).

37. Shea, T., Costa, F., Krimer, D. & Hammer, J. E. Accuracy of timescales retrieved from diffusion modeling in olivine: A 3D perspective. *American Mineralogist* **100**, 2026–2042 (2015).

38. Gudmundsson, M. T. *et al.* Gradual caldera collapse at Bárarbunga volcano, Iceland, regulated by lateral magma outflow.*Science* **353**, aaf8988 (2016).

39. Anderson, A. CO_2 and the eruptibility of picrite and komatiite. *Lithos* **34**, 19–25 (1995).

40. White, R. S. *et al.* Dynamics of dyke intrusion in the mid-crust of Iceland. *Earth and Planetary Science Letters* **304**, 300–312 (2011).

41. Hooper, A. *et al.* Increased capture of magma in the crust promoted by ice-cap retreat in Iceland. *Nature Geoscience* **4**, 783 (2011).

42. Tarasewicz, J., Brandsdóttir, B., White, R. S., Hensch, M. & Thorbjarnardóttir, B. Using microearthquakes to track repeated magma intrusions beneath the Eyjafjallajökull stratovolcano, Iceland. *Journal of Geophysical Research: Solid Earth* **117**, B9 (2012).

43. Hudson, T. *et al.* Deep crustal melt plumbing of Bárarbunga volcano, Iceland. *Geophysical Research Letters* **44**, 8785-8794 (2017).

44. Key, J., White, R. S., Soosalu, H. & Jakobsdóttir, S. S. Multiple melt injection along a spreading segment at Askja, Iceland. *Geophysical Research Letters* **38**, 5 (2011).

45. Aiuppa, A. *et al.* Unusually large magmatic CO_2 gas emissions prior to a basaltic paroxysm. *Geophysical Research Letters* **37**, 17 (2010).

46. Bali, E., Hartley, M., Halldórsson, S., Gudfinnsson, G. & Jakobsson, S. Melt inclusion constraints on volatile systematics and degassing history of the 2014–2015 Holuhraun eruption, Iceland. *Contributions to Mineralogy and Petrology* **173**, 9 (2018).

47. Schwandner, F. M. *et al.* Spaceborne detection of localized carbon dioxide sources. *Science* **358**, eaam5782 (2017).

48. Chiodini, G., Cioni, R., Guidi, M., Raco, B. & Marini, L. Soil CO_2 flux measurements in volcanic and geothermal areas. *Applied Geochemistry* **13**, 543–552 (1998).

49. Shishkina, T., Botcharnikov, R., Holtz, F., Almeev, R. & Portnyagin, M. V. Solubility of H_2O- and CO_2-bearing fluids in tholeiitic basalts at pressures up to 500 MPa. *Chemical Geology* **277**, 115–125 (2010).

50. Vergniolle, S. & Jaupart, C. Separated two-phase flow and basaltic eruptions. *Journal of Geophysical Research: Solid Earth* **91**, 12842–12860 (1986).

51. Poland, M. P., Miklius, A., Sutton, A. J. & Thornber, C. R. A mantle-driven surge in magma supply to Kīlauea Volcano during 2003–2007. *Nature Geoscience* **5**, 295 (2012).

52. Bradshaw, R. W. & Kent, A. J. The analytical limits of modeling short diffusion timescales. *Chemical Geology* **466**, 667–677 (2017).

53. QUANTAX. *CrystalAlign* (Bruker Nano GmbH,Berlin, Germany, 2010).

54. Bachmann, F., Hielscher, R. & Schaeben, H. Texture analysis with MTEX–free and open source software toolbox. In *Solid State Phenomena*, vol. 160, 63–68 (Trans Tech Publ, 2010).

55. MATLAB. *version 9.10.0 (R2016b)* (The MathWorks Inc.,Natick, Massachusetts, 2016).

56. Coogan, L., Hain, A., Stahl, S. & Chakraborty, S. Experimental determination of the diffusion coefficient for calcium in olivine between 900 °C and 1500 °C.*Geochimica et Cosmochimica Acta* **69**, 3683–3694 (2005).

57. Ito, M. & Ganguly, J. Diffusion kinetics of Cr in olivine and ^{53}Mn–^{53}Cr thermochronology of early solar system objects. *Geochimica et Cosmochimica Acta* **70**, 799–809 (2006).

58. Oeser, M., Ruprecht, P. & Weyer, S. Combined Fe-Mg chemical and isotopic zoning in olivine constraining magma mixing-to-eruption timescales for the continental arc volcano Irazú (Costa Rica) and Cr diffusion in olivine. *American Mineralogist* **103**, 582–599 (2018).

59. Jollands, M. *et al.* Substitution and diffusion of Cr^{2+} and Cr^{3+} in synthetic forsterite and natural olivine at 1200–1500 °C and 1 bar. *Geochimica et cosmochimica acta* **220**, 407–428 (2018).

60. Costa, F., Dohmen, R. & Chakraborty, S. Time scales of magmatic processes from modeling the zoning patterns of crystals. *Reviews in Mineralogy and Geochemistry* **69**, 545–594 (2008).

61. Yang, H.-J., Kinzler, R. J. & Grove, T. Experiments and models of anhydrous, basaltic olivine-plagioclase-augite saturated melts from 0.001 to 10 kbar. *Contributions to Mineralogy and Petrology* **124**, 1–18 (1996).

62. Kress, V. C. & Carmichael, I. S. The compressibility of silicate liquids containing Fe_2O_3 and the effect of composition, temperature, oxygen fugacity and pressure on their redox states. *Contributions to Mineralogy and Petrology* **108**, 82–92 (1991).

63. Ghiorso, M. S. & Sack, R. O. Chemical mass transfer in magmatic processes IV. a revised and internally consistent thermodynamic model for the interpolation and extrapolation of liquid-solid equilibria in magmatic systems at elevated temperatures and pressures. *Contributions to Mineralogy and Petrology* **119**, 197–212 (1995).

64. Gualda, G. A., Ghiorso, M. S., Lemons, R. V. & Carley, T. L. Rhyolite-MELTS: a modified calibration of melts optimized for silica-rich, fluid-bearing magmatic systems. *Journal of Petrology* **53**, 875–890 (2012).

65. Sigurdsson, I. A., Steinthorsson, S. & Grönvold, K. Calcium-rich melt inclusions in Cr-spinels from Borgarhraun, northern Iceland.*Earth and Planetary Science Letters* **183**, 15–26 (2000).

66. Girona, T. & Costa, F. DIPRA: A user-friendly program to model multi-element diffusion in olivine with applications to timescales of magmatic processes. *Geochemistry, Geophysics, Geosystems* **14**, 422–431 (2013).

67. Chakraborty, S. Diffusion coefficients in olivine, wadsleyite and ringwoodite. *Reviews in mineralogy and geochemistry* **72**, 603–639 (2010).

68. Costa, F. & Morgan, D. Time constraints from chemical equilibration in magmatic crystals. *Timescales of Magmatic Processes: From Core to Atmosphere* 125–159 (2010).

69. Meißner, E. *Messung von kurzen Konzentrationsprofilen mit Hilfe der analytischen Transmissionselektronenmikroskopie (TEM-EDX) am Beispiel der Bestimmung von Diffusionskoeffizienten für die Mg-Fe-Interdiffusion in Olivin. Ph.D. thesis, Universität Bayreuth, Fakultät für Biologie, Chemie und Geowissenschaften* (2000).

70. Feroz, F., Hobson, M., Cameron, E. & Pettitt, A. Importance nested sampling and the MultiNest algorithm. *arXiv preprint arXiv:1306.2144* (2013).

71. Buchner, J. *et al.* X-ray spectral modelling of the AGN obscuring region in the CDFS: Bayesian model selection and catalogue. *Astronomy & Astrophysics* **564**, A125 (2014).

72. Crank, J. *The mathematics of diffusion* (Oxford university press, 1979).

73. Paquet, F., Dauteuil, O., Hallot, E. & Moreau, F. Tectonics and magma dynamics coupling in a dyke swarm of Iceland. *Journal of Structural Geology* **29**, 1477–1493 (2007).

74. Lange, R. & Carmichael, I. S. Thermodynamic properties of silicate liquids with emphasis on density, thermal expansion and compressibility. *Reviews in Mineralogy and Geochemistry* **24**, 25–64 (1990).

75. Giordano, D., Russell, J. K. & Dingwell, D. B. Viscosity of magmatic liquids: a model. *Earth and Planetary Science Letters* **271**, 123–134 (2008).

76. Thordarson, T. & Self, S. The Laki (Skaftár Fires) and Grímsvötn eruptions in 1783–1785. *Bulletin of Volcanology* **55**, 233–263 (1993).